Applied Energy 375 (2024) 123972

Contents lists available at ScienceDirect

Applied Energy

journal homepage: www.elsevier.com/locate/apenergy

Modeling, optimization and comparative assessment of power-to-methane and carbon capture technologies for renewable fuel production

Oscar Furst [a], Lukas Wehrle [a], Daniel Schmider [b], Julian Dailly [b], Olaf Deutschmann [a,*]

[a] Karlsruhe Institute of Technology, Kaiserstraße 12, Karlsruhe, 76131, Baden-Württemberg, Germany
[b] European Institute for Energy Research, Emmy-Noether-Straße 11, Karlsruhe, 76131, Baden-Württemberg, Germany

GRAPHICAL ABSTRACT

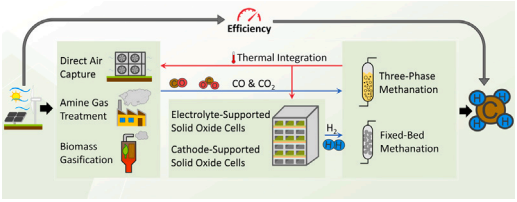

ARTICLE INFO

Keywords:
Power-to-methane
Solid oxide electrolysis cells
Catalytic methanation
Direct air capture
Amine gas treatment
Biomass gasification

ABSTRACT

Power-to-X systems which convert electrical energy into stable chemical energy carriers are a promising solution to the long-term energy storage challenge posed by the increasing market penetration of intermittent renewable power sources. In this paper, a systematic and flexible method for optimizing the steady-state operating conditions of Power-to-Methane (PtM) plant concepts is showcased and applied to perform a comparative assessment of a multitude of PtM process chains. As opposed to existing studies, a large number of comprehensive PtM system models integrating multiple carbon capture technologies and Solid Oxide Electrolysis Cell (SOEC) stacks are optimized. Using detailed 3D SOEC stack simulations and interpolation-based model reduction, the performance of electrolyte-supported (ESC) and cathode-supported cells (CSC) integrated in a variety of PtM systems with air and pure oxygen sweep gas concepts is compared. A total of 20 plant concepts using different combinations of carbon capture (biomass gasification, amine gas treatment, direct air capture) and methanation (fixed-bed, slurry bubble column) technologies are investigated using the pinch method. The results demonstrate that thermal integration of the carbon capture process in PtM systems can raise the total efficiency of the process chains by up to 10.9% for direct air capture and 10.4% for amine gas treatment, with the plants reaching high heating value efficiencies of 70.2% and 84.6% respectively. Endothermic, high temperature operation of SOECs is shown to consistently yield the highest PtM efficiencies due to the minimization of cell overpotentials and power inverter losses. Conversely, exothermic operation of SOECs thermally integrated with energy-intensive carbon capture processes is shown to significantly lower capital expenditures (CAPEX) while incurring an efficiency loss lower than 1% compared to thermoneutral operation.

* Corresponding author.
E-mail addresses: oscar.furst@kit.edu (O. Furst), lukas.wehrle@kit.edu (L. Wehrle), daniel.schmider@eifer.org (D. Schmider), dailly@eifer.org (J. Dailly), deutschmann@kit.edu (O. Deutschmann).
URL: https://www.itcp.kit.edu/deutschmann/ (O. Deutschmann).

https://doi.org/10.1016/j.apenergy.2024.123972
Received 16 October 2023; Received in revised form 10 June 2024; Accepted 19 July 2024
Available online 7 August 2024
0306-2619/© 2024 The Authors. Published by Elsevier Ltd. This is an open access article under the CC BY license (http://creativecommons.org/licenses/by/4.0/).

Nomenclature

Abbreviations

3PM	Three-phase methanation
AGT	Amine gas treatment
BG	Biomass gasification
CAPEX	Capital expenditure
CC	Carbon capture
CNG	Compressed natural gas
CSC	Cathode-supported cell
DAC	Direct air capture of CO2
ESC	Electrolyte-supported cell
FBM	Fixed bed methanation
HHV	High heating value
OPEX	Operating expense
PEM	Polymer electrolyte membrane
PtM	Power to methane
RU	Repeating unit
SNG	Synthetic natural gas
SOC	Solid oxide cell
SOEC	Solid oxide electrolysis cell

Sub- and superscripts

blow	Blower
cool	Methanation unit coolant
elec	Electric
in	Inlet
meth	Methanation
out	Outlet

Physical quantities

$\dot{m}$	Mass flow rate
$\dot{V}$	Volumetric flow rate
η	Efficiency
ϕ	Sweep gas to fuel ratio
E	Voltage
i	Current density
P	Power
p	Pressure
Q	Heat
SC	Steam conversion
T	Temperature

1. Introduction

In order to mitigate global emissions of greenhouse gasses, renewable energy production grows consistently, albeit slowly, across the globe. On average, the proportion of renewable energies in the primary energy supply of OECD countries has risen by 4 percentage points (pp) between 2010 and 2020, reaching 7.9% in the USA, 9.68% in China and 15.18% in the European Union [1].

Power-to-X systems which convert electrical energy into chemical energy carriers address the lack of long-term energy storage posed by the increasing market penetration of intermittent renewable power sources and the decarbonization of hard-to-abate industrial sectors [2–4].

While electrolytic hydrogen is the cornerstone of Power-to-Gas systems, further processing into products with higher volumetric energy density, like methane (22.2 $MJ\,L^{-1}$) [5], methanol (15.6 $MJ\,L^{-1}$) [6], ammonia (11.5 $MJ\,L^{-1}$) [7] or formic acid (6.4 $MJ\,L^{-1}$) [8–10], helps to cover the needs of a broader range of end-users (energy densities referring to the liquid state). Hydrogen is also used in emergent solid-state energy storage technologies through reduction of iron oxides (40.7 $MJ\,L^{-1}$) [11,12] or direct storage in metal hydrides [13,14], but these storage methods suffer from low gravimetric energy densities.

Due to the consistent demand for natural gas [15], the existing infrastructure [16] and the emerging need for sustainable fuels in the transportation sector [17], the Power-to-Methane (PtM) process, which converts electricity into synthetic natural gas (SNG) via electrolysis, carbon capture and methanation, is a promising technology for the renewable production of a versatile compound [18]. Compared to other hydrocarbons, methane has the highest hydrogen to carbon ratio, resulting in a high volumetric energy density and low CO_2 emissions.

Owing to the low maturity of the technology, only pilot-scale PtM plants are operated, with the installed capacity totaling 47 MW_{el} worldwide as of 2019 [19]. Multiple projects demonstrating methane production through biogas upgrading were launched since 2011 [20–23]. The HELMETH project [24], which ran from 2014 to 2017, was the first to demonstrate thermal integration of pressurized Solid Oxide Electrolysis Cell (SOEC) stacks (10 kW, 15 bar) with fixed bed catalytic methanation reactors. Presupposing optimization of process conditions and heat losses, system high heating value (HHV) efficiencies were projected to reach 80%.

Lowering the cost of the produced SNG requires an improvement of the dynamic operation capability of plants, increase of the process efficiency and decrease of the electrolyzer capital expenditures (CAPEX) [25,26]. Therefore, all technologies available for the electrolysis, carbon capture and methanation processes that constitute a PtM system are under active development.

Solid Oxide Electrolysis Cells (SOECs) are in the demonstration stage (TRL7 according to the International Energy Agency in 2022) [27]. The deployment of efficient high-temperature electrolyzers with progressively higher capacities, e.g., the 720 kW unit operated by the Salzgitter AG [28] and the more recent 2.6 MW SOEC by Sunfire [29], demonstrate the growing interest in the technology. They offer an excellent electrical efficiency [30–32], which reaches 84% (based on the lower heating value (LHV) of H_2) in commercial units, producing hydrogen at 3.6 $kWh\,N\,m^{-3}$ [33], compared to 4.5 $kWh\,N\,m^{-3}$ [34] for PEM and 3.8 $kWh\,N\,m^{-3}$ [35,36] for alkaline electrolyzers. In addition, high system efficiencies can be achieved by coupling SOECs with the exothermic methanation process due to the advantageous thermal integration [37] and possibility of CO_2-electrolysis [38]. Apart from process integration, current research on SOECs has a strong focus on performance and durability improvements through the development of new and improved electrode and electrolyte materials [39].

Carbon capture (CC) technologies, which allow the separation of CO_2 from gases, are crucial components in order to reach a low-carbon economy [4,40], designed and implemented as parts of a large variety of carbon capture, utilization and storage systems [41]. The viability of the wide range of commercially available CC technologies is mostly dependent on geographical factors [42,43], which include the local presence of stationary CO_2 emitters, availability of waste heat and electricity costs. For the decarbonization of hard-to-abate industries, CO_2 can be captured from flue gases [4] with technologies such as Amine Gas Treatment (AGT), in which organic solvents like monoethanolamine (MEA) are used to absorb CO_2 to form weakly bonded chemical compounds that can be regenerated using heat [44]. For the CO_2 removal from the atmosphere, CC through the sustainable production of carbon-rich biomass is promising due to its ability to provide energy [45] and valuable industrial feedstock [4] after processing, e.g., synthesis gas obtained through biomass gasification (BG) or biogas production through anaerobic digestion [46] and subsequent pyrolysis [47]. However, the high land-use of biomass-based solutions, which compete with food production [48], leaves room for more expensive technological alternatives like Direct Air Capture (DAC) [49],

which enable the separation of CO_2 from air using physical adsorption on solid sorbent materials and later regeneration through heat and/or vacuum [50,51].

Methanation, which is a key technology in carbon capture and utilization processes [4], can be performed biologically and catalytically. Biological methanation reactors use microbial cultures to turn biogas into methane at low temperatures and have the advantage of being robust against feedstock impurities [52]. Catalytic methanation in Fixed-Bed Methanation (FBM) reactors is a well-established technology [53,54] and is now considered for the production of SNG. In order to improve the dynamic behavior of catalytic methanation reactors, alternative reactor types have been developed to address the heat management issues of FBM [55], e.g., Three-Phase Methanation (3PM) reactors [56,57] and honeycomb reactors [58].

Due to the large variety of available PtM processes [59,60] and the complex interactions between processes of thermally integrated plants, the performance and optimal design-point of plant concepts composed of selected electrolysis, methanation and CC technologies is not easily determined. PtM plant models are useful to evaluate the energetic efficiency and economic viability of plant concepts. Therefore, modeling of such plants is a dynamic research field. Several studies perform a detailed investigation of a specific plant design using multi-scale models for most system components [25,37,61,62], sometimes coupled to optimization algorithms in order to determine optimal operating conditions [38,63–66]. On the other hand, simplified modeling approaches are used by some researchers in order to perform comparative assessments between different plant concepts [67] or more complex optimization tasks, such as solving scheduling problems for the dynamic operation of plants powered by intermittent renewable energy sources [5,68–71]. In order to enable the use of multi-physics component models for computationally intensive optimization studies, Chi et al. [72,73] demonstrated the use of surrogate SOEC models calibrated on detailed simulation data.

However, such SOEC surrogate models have not yet been leveraged to include more accurate 3D stack models in PtM process optimizations. PtM system optimization studies commonly assume fixed electrolyzer operating conditions and therefore cannot study energetic trade-offs and synergies between electrolyzer and methanation reactor operating conditions [68,71,74,75]. At most, studies include simple 0D or 1D electrolyzer models [69,76] which allow the optimization of a small subset of the electrolyzer operating parameters.

Additionally, literature on integration of CC technologies into PtM systems is scarce. While the integration of PtM systems with the BG process has been studied [37,68,75,77], DAC and AGT integration has only been studied in combination with PEM electrolysis [76,78,79]. The majority of PtM system studies, especially optimizations, assume an upstream CO_2 separation process which is independent of the PtM plant and provides a stable supply of CO_2 [69–71,74,80].

In this paper, a systematic and flexible method for optimizing the steady-state operating conditions of PtM process chains is showcased. The method is based on a combination of process simulation, pinch analysis and derivative-free multivariate optimization. Process simulation is used to determine the material and energetic interactions between plant components by solving mass and energy conservation equations. Pinch analysis is used to evaluate the highest achievable efficiency of the plant concepts. Finally, multivariate optimization is used to determine the optimal operating conditions that maximize the energy efficiency of the process chains.

The selected methodology is used to conduct a comparative assessment of PtM plant concepts using SOEC stacks for hydrogen production via steam electrolysis [39]. Using multi-physics 3D SOEC stack models [81,82] built upon electrolyte-supported (ESC) and cathode-supported (CSC) cell designs, aided by interpolation-based model reduction, fully-integrated simulations of processes comprising different CC technologies (BG, AGT, DAC) and catalytic methanation technologies (FBM, 3PM) are performed.

This study aims to elucidate synergies among process components and identify energetically advantageous trade-offs by comparing optimized process chains. These insights aspire to deepen our understanding of how operating certain process components under sub-optimal conditions can enhance the overall energy balance of PtM plants. By uncovering these process interdependencies, this work can contribute to the design of plants that are more commercially viable. By optimizing energy use throughout the plant, PtM facilities can reduce their operational costs and become more competitive in the renewable energy sector.

The novelties provided by this study include the (i) systematic optimization and comparative energy assessment of a large number of PtM process chains (ii) with material and thermal integration of multiple CC technologies, notably the amine gas treatment and direct air capture processes whose thermal integration with SOECs, according to the author's best knowledge, have not been reported yet in the literature. (iii) The benefit of CC thermal integration in PtM process chains is evaluated by comparison with isolated CC and PtM processes simulated using the same methodology. (iv) Simultaneously, a detailed stack model is used to compare the performance of CSCs and ESCs, both standalone and integrated in PtM systems.

2. Methodology

The optimization of the PtM plant concepts is implemented in three abstraction layers depicted in Fig. 1: the individual plant component models, the fully integrated plant simulation and the optimization algorithm. Hereafter, these layers and their interactions are explained.

2.1. System simulation

Power-to-methane plants are built around a methanation process, which produces methane-rich SNG from CO, CO_2 and H_2. The product SNG is then dried and conditioned for storage, transport or direct use [83–85]. The structure of PtM process chains is schematically depicted in Fig. 2.

Multiple PtM system concepts are investigated in this paper, which are realized by combining the different methanation, electrolysis and carbon capture technologies listed in Table 1. Fig. 3 illustrates the process chain for a plant concept using CO_2 from AGT, the 3PM unit and using air as a sweep gas in the SOEC. Plant concepts containing the remaining technologies considered in this study can be found in Appendix A. Detailed descriptions, process diagrams and modeling methodology of all considered technologies are in Section 2.2.

In order to simulate different power-to-SNG plant concepts under various operating conditions, a flexible simulation tool was developed in Matlab. From a given set of methanation, electrolysis and carbon capture technologies, the tool produces a full plant model by selecting the necessary intermediary conditioning processes: (i) The CO_2, syngas, H_2, electrolyzer sweep gas (air or oxygen) and SNG are dried, compressed and/or expanded according to the subsystem operating conditions. (ii) The balance between steam produced through methanation reactor cooling and utilized in the electrolyzer and BG unit is computed and any deficit is compensated by an additional steam source. (iii) Additionally the SNG output of every plant concept is dried to 50 $\mathrm{mg\,N\,m^{-3}}$ H_2O, which is the requirement for compressed H-gas in Germany [86], and compressed to 200 bar, which corresponds to the pressure of CNG used in vehicles [87].

In order to quantitatively compare the performance of the different plant configurations (i.e., combinations of main process technologies and specific operating conditions), an energetic assessment of each concept is performed by means of thermal integration. The comparability of the results is ensured through the use of the pinch method [88], which enables the computation of the heating and cooling requirements of a perfectly thermally integrated plant. In this study, the hot utility is assumed to be provided by 100% efficient electrical heaters [37,65],

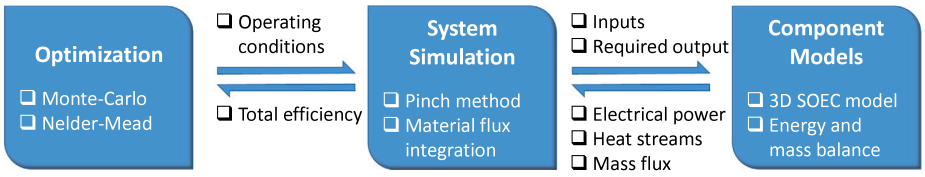

Fig. 1. Diagram of the hierarchy and relationship between the three abstraction layers of the modeling and optimization methodology.

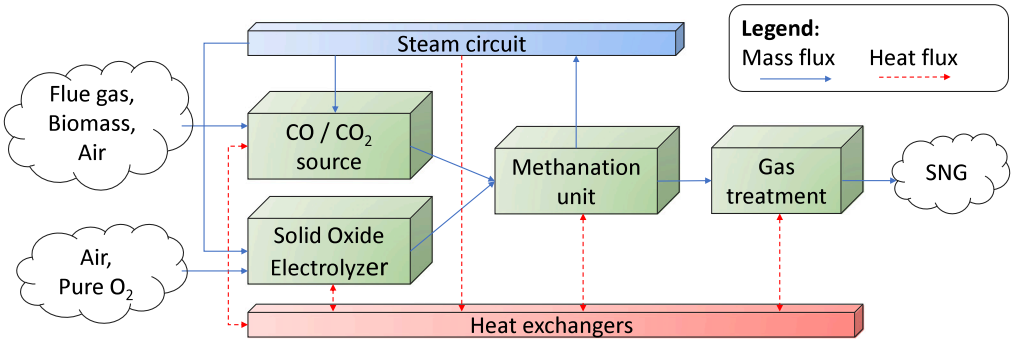

Fig. 2. Schematic representation of the main process components of thermally integrated power-to-methane plants.

Table 1
Summary of the different technologies assessed for the electrolysis, methanation and carbon capture with their respective optimization variables.

Process	Technologies	Variables	Range
Electrolysis	Cathode supported Electrolyte supported	Pressure Inlet temperature Current density Steam conversion Air-to-fuel ratio	1–20 bar 1073–1173 K (ESC) 923–1023 K (CSC) 0.3–1.2 A cm^{-2} (ESC) 0.3–1.5 A cm^{-2} (CSC) 70%–90% 1–6
Methanation	Fixed catalyst bed Slurry bubble column	Inlet temperature Pressure Coolant pressure	523–623 K 1–30 bar 1–30 bar
Carbon capture	Biomass gasification	Gasifier pressure	1 and 20 bar
	Amine gas treatment Direct air capture	No parameter with significant interactions with other process components, state-of-the-art process is used.	

while the cold utility is assumed to be available at 293 K. A minimal temperature difference between heating and cooling medium of $\Delta T_{min} = 20$ K was defined [37,89,90], which limits the size of the heat exchanger used at the pinch point.

Anghilante et al. [37] comparatively assessed system efficiencies of several Power-to-SNG bio-syngas-based plant concepts, which were either computed via the pinch method, or via a full explicit thermal integration using a functional, yet conservative heat exchanger layout. Modeled discrepancies between the two approaches were found to be below 2 pp for all cases, emphasizing that pinch analysis provides an upper, yet representative Power-to-SNG efficiency computation. Due to the congruent numerical approach, similar discrepancies are expected for the simulations performed in this work.

Following the pinch analysis, the efficiency of a plant η_{HHV} is computed through Eq. (1), which includes the HHV of the produced SNG (at least 95% CH_4, up to 2% H_2 and residual amounts of CO and C_2H_4) HHV_{SNG}, the heating requirement as computed by the pinch analysis $P_{heating}$, the electrical power consumption of all plant components $\sum P_{elec}$ and the HHV of the feedstock used in the gasification unit $HHV_{biomass}$ if present.

$$\eta_{HHV} = \frac{HHV_{SNG}}{P_{heating} + \sum P_{elec} + HHV_{biomass}} \quad (1)$$

2.2. System component models

For the system model to be able to perform the thermal integration and compute the PtM efficiency, each component model needs to produce the following set of information: temperature and enthalpy of the required heat stream $T_{cold}(Q)$, available heat stream $T_{hot}(Q)$, electrical power consumption P_{elec} and outlet properties (mole fractions X_{out}, mass flow $\dot{m}_{out}$, pressure p_{out}, temperature T_{out}). These results are functions of the inlet properties (mole fractions X_{in}, mass flow $\dot{m}_{in}$, pressure p_{in}^{SOEC}, temperature T_{in}^{SOEC}) and operating conditions found in Table 1.

In this section, all subsystem models are introduced, accompanied by process diagrams in which the cold streams and hot streams considered in the pinch analysis are depicted as heaters and coolers respectively.

2.2.1. Carbon capture

Contrary to the majority of PtM system models [25,65,71,91,92], in the present approach, the CC technology is integrated in the plant. The considered CC technologies, which supply carbon monoxide and carbon dioxide to the methanation process, are BG, AGT and DAC. This allows thermal and material integration with the other plant components, which is beneficial for all selected CC technologies: DAC and AGT require large amounts of low-temperature heat [93,94], while

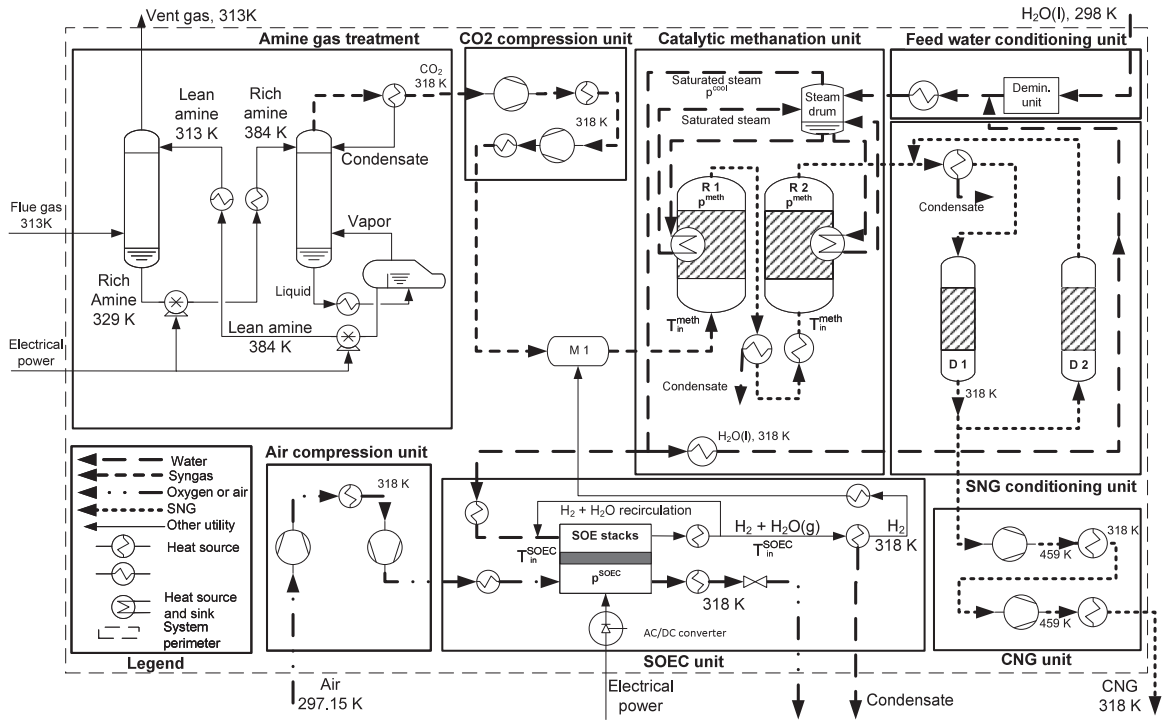

Fig. 3. Power-to-gas process chain with AGT, 3PM and without SOEC sweep gas recirculation.

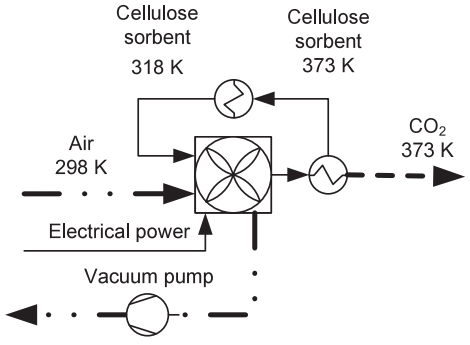

Fig. 4. Direct air capture process diagram.

autothermal BG utilizes the high-temperature oxygen produced by the electrolyzer to produce nitrogen-lean syngas [95].

Direct air capture (DAC) captures CO_2 (and approximately 0.5% water vapor [96]) from the ambient air. The chosen DAC technology, which is commercially applied by Climeworks [93], is based on the temperature-vacuum swing process using an amine-functionalized cellulose sorbent to separate CO_2 from the ambiant air. In this cyclic process, air is first circulated through the adsorbent bed until the sorbent is saturated. The sorbent bed is then evacuated. After heating up the sorbent to 373 K, the adsorbed CO_2 is released and can be isolated. In our model, the semi-batch process is implemented in a continuous form by the equivalent stationary model depicted in Fig. 4, which was designed to yield identical results to a cyclic model averaged over time.

Heat streams are computed using material properties of amine-functionalized cellulose sorbent published by Wurzbacher et al. [96] and provided in Table 2. The electricity consumption of the DAC unit was assumed to be directly proportional to the amount of CO_2 produced, at 1.8 MJ $kg_{CO_2}^{-1}$, with data released by Climeworks [93] used as reference. The same reference predicts a thermal power consumption

Table 2
Selected amine-functionalized cellulose sorbent properties [96].

Property	Unit	Value
Specific heat capacity	kJ kg^{-1} K^{-1}	$c_p^{ads} = 2.07$
CO_2 loading (48% humidity)	mol kg^{-1}	$q_{CO_2} = 1.222$
H_2O loading (48% humidity)	mol kg^{-1}	$q_{H_2O} = 3.0$
CO_2 adsorption enthalpy	kJ mol^{-1}	$\Delta H_{ads,CO_2} = 60$
H_2O adsorption enthalpy	kJ mol^{-1}	$\Delta H_{ads,H_2O} = 49$

of 5.4 MJ $kg_{CO_2}^{-1}$ for their optimized systems, matched closely by the pinch analysis of the present model which yields 5.34 MJ $kg_{CO_2}^{-1}$.

Amine gas treatment (AGT) is a technology that is used to separate CO_2 (and approximately 10% water vapor [94]) from flue gases. A piperazine activated methyldiethanolamine (45 wt.% MDEA/5 wt.% PZ) solution was chosen as CO_2 sorbent in this analysis because its CO_2 absorption reaction has a low enthalpy (≈70 kJ $mol_{CO_2}^{-1}$) and fast kinetics [94,97–99]. The component model, depicted in Fig. 5, is adapted from the detailed numerical analysis by Zhao et al. [94], which was used as reference for the process, the material properties of the solvent and the eclectic power consumption of 13.5 kJ $kg_{CO_2}^{-1}$. The study assumes a flue gas composition of 12 vol.% CO_2, 78 vol.% N_2 and 10 vol.% H_2O which corresponds to the output of a coal-fired power plant after treatment. The pinch analysis of the simplified model with ΔT_{min} = 10 K yields a minimum thermal power consumption of 2.8 MJ $kg_{CO_2}^{-1}$ compared to 3.3 MJ $kg_{CO_2}^{-1}$ (captured CO_2) in the referenced explicit thermal integration. With the pinch temperature ΔT_{min} = 20 K used herein, the predicted heat requirement is 3.7 MJ $kg_{CO_2}^{-1}$.

Trace amounts of hydrogen sulfide (H_2S) can be present in the AGT output (depending on the flue gas composition), which acts as a catalyst poison for the methanation reactor [100]. Therefore, the output is cleaned in a ZnO column, for which the gas is heated to 593 K [101].

Biomass gasification (BG) with subsequent gas cleaning and impurity separation (see Fig. 6) is a process that converts carbon-based organic materials (e.g., wood chips or straw) into a mixture consisting of H_2, CO, CO_2, CH_4 and steam (syngas).

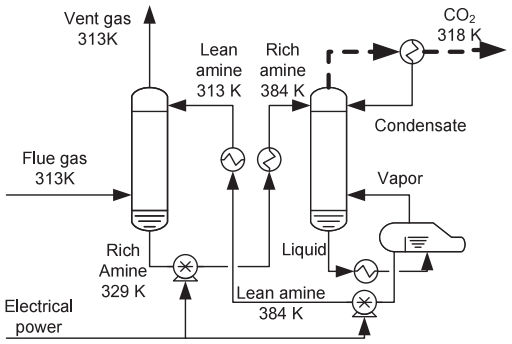

Fig. 5. Amine gas treatment process diagram.

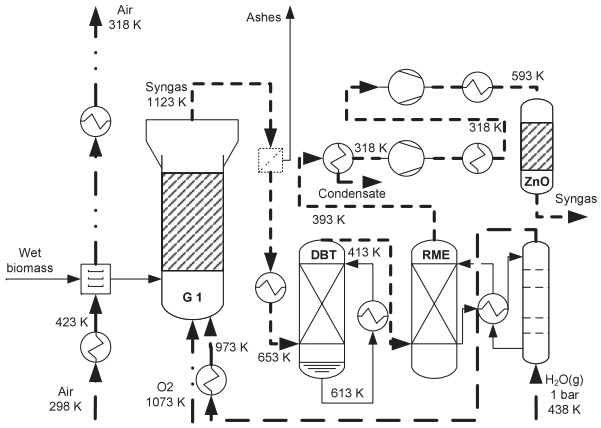

Fig. 6. Gasification process diagram.

The biomass gasification model herein is based on literature data from wood (the most widespread source of biomass on the market [102,103]) gasification experiments under autothermal conditions leading to low tar concentrations [95,104], achieved through the addition of steam (steam/carbon ratio = 1) and oxygen (equivalence ratio = 0.25). The resulting syngas composition and temperature is provided for gasification at 1 bar and 20 bar, which were treated as fixed setpoints in this study due to a lack of experimental data at intermediate pressure levels.

In the present model, the required oxygen is provided by the SOEC and a gas expander is placed between the SOEC and BG unit if the electrolysis module is operated under elevated pressure. Unless specified otherwise, the presented results were obtained with gasification at 1 bar.

For the production of syngas in a plant producing 20 MW of methane, approximately 10.5 MW (HHV) of wood is required with a power consumption of 208 kW for drying, which is congruent with the study of Anghilante et al. [37] with 10.8 MW (HHV) and 210 kW respectively.

The gasifier output contains a significant amount of contaminants, including H_2S (0.01%), tar (0.2%) and Ashes (0.04%) [105]. Therefore, the gas is treated in multiple steps. First, the ashes are removed using a filter. Then, a dibenzyltoluene (DBT) cleaning unit and rapeseed methyl ester (RME) cleaning unit remove Tar and the majority of H_2S [104]. The remaining H_2S is then removed in a ZnO column [101].

2.2.2. Catalytic methanation reactor

Catalytic methanation reactors convert CO, CO_2 and H_2 into methane and steam through the Sabatier, CO-methanation and water gas shift reactions (Eqs. (2)–(4)) in presence of a catalyst, usually Nickel [106].

$$CO_2 + 4\,H_2 \longleftrightarrow CH_4 + 2\,H_2O \qquad \Delta H_R = -165\ \mathrm{kJ\,mol^{-1}} \tag{2}$$

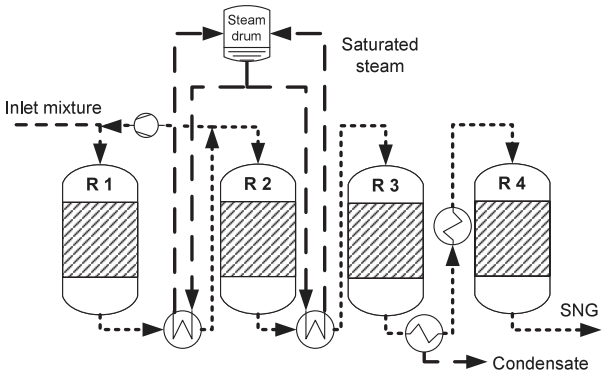

Fig. 7. Fixed-bed methanation process diagram.

$$CO + 3\,H_2 \longleftrightarrow CH_4 + H_2O \qquad \Delta H_R = -206\ \mathrm{kJ\,mol^{-1}} \tag{3}$$

$$CO + H_2O \longleftrightarrow CO_2 + H_2 \qquad \Delta H_R = -41\ \mathrm{kJ\,mol^{-1}} \tag{4}$$

Methanation reactors perform best below 823 K to favor methane formation and avoid deactivation of the catalyst by sintering and carbon formation temperatures above 673 K reduce the ethane selectivity and prevent the formation of nickel carbonyl. Further, elevated pressures improve CO and CO_2 conversion [56]. Since the methanation process is highly exothermic, reaction heat removal is crucial to the stability of the catalyst and improves the thermodynamic equilibrium of the reaction [56]. Heat can be removed effectively by cooling pipes using pressurized water as working fluid, taking advantage of two-phase heat transfer while also producing steam [104].

In order to reasonably limit the computational requirements of the system analysis, every methanation reactor is assumed to yield chemical equilibrium at its output, computed through Gibbs free energy minimization. The gas input into the methanation unit consists of a stoichiometric mixture of dried CO_2 or syngas and electrolytic H_2. For both reactor designs, the reaction heat is recovered by a steam circuit, which produces the superheated steam needed for the SOEC.

Two types of catalytic methanation reactors, and corresponding processes, are considered in this study: FBM reactors and 3PM slurry bubble column reactors.

Fixed-bed methanation (FBM) reactors, which are an established technology for carbon oxide removal in process gases [53,55], operate adiabatically and the reaction heat is removed from the product gas. The process chosen for the FBM unit, shown in Fig. 7, is analogous to the Haldor Topsoe TREMP process, consisting of four reactors with intermediate cooling and recirculation of the first reactor output [107]. Adiabatic reactor operation is assumed, whilst imposing an equivalent inlet gas temperature $T_{\mathrm{in}}^{\mathrm{meth}}$ and operating pressure $p_{\mathrm{in}}^{\mathrm{meth}}$ for all reactors, which are both set as optimization variables. Compared to experimental results of Schaaf et al. [56] on a single FBM reactor with an inlet temperature of 523 K, 20 bar and 27.7 vol.% CH_4, 33.8 vol.% H_2, 8.5 vol.% CO_2, 30.0 vol.% H_2O gas composition, which attained a CO_2 conversion of 64%, the adiabatic equilibrium model predicts a conversion of 66%.

The cooling between the first three reactors is performed by the steam circuit and returns the gas to the appropriate inlet temperature $T_{\mathrm{in}}^{\mathrm{meth}}$ with only small amounts of condensation. Before entering the last reactor, the process gas is dried by cooling to 319 K, which further increases the final methane yield. The dried gas is then reheated to $T_{\mathrm{in}}^{\mathrm{meth}}$ before entering the fourth reactor.

Three-phase methanation (3PM) reactors are filled with an inert cooling fluid, e.g., dibenzyltoluene, which allows heat removal from within the reactor and isothermal operation [55,57,108]. Both the thermodynamics and the dynamic operation capability benefit from the improved

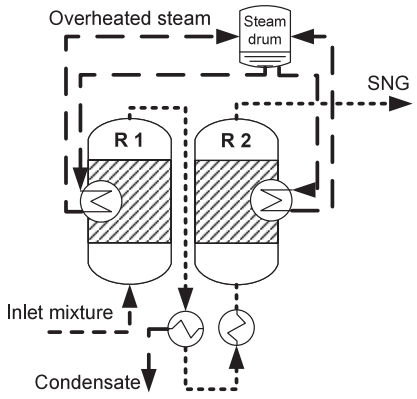

Fig. 8. Three-phase methanation process diagram.

thermal management across the reactor [109,110], which is crucial for PtM plants designed to adapt to the intermittent renewable electricity supply. The selected process, shown in Fig. 8 is composed of two reactors, with a single condensation and reheating step in between [37, 104]. In this reactor concept, the steam circuit directly recovers the reaction heat while maintaining a constant temperature $T_{\text{in}}^{\text{meth}}$ in the reactors. Although the isothermal equilibrium model overestimates the conversion of 3PM reactors, predicting close to full CO_2 conversion at 593 K and 20 bar for a stoichiometric mixture as opposed to 82% [111], the two-step process is anticipated to achieve near-complete conversion. Due to isothermal operation, the integration of heat streams from both reactors in the pinch analysis implies minimal disparity in plant efficiency whether conversion is attained through one or two reactors.

2.2.3. Solid oxide electrolysis cell (SOEC) stacks

The SOECs used for H_2 production in the analyzed plant concepts utilize the steam produced from the methanation process, which significantly reduces the amount of heating required to operate the electrolyzer. Herein, the performance of two SOEC architectures is compared: electrolyte-supported cells (ESC) and cathode-supported cells (CSC).

In ESCs, the mechanical stability of the cell is provided by a thick electrolyte layer, which simplifies the manufacturing of the cells and provides a durable seal against gas leakage. However, the thick electrolyte increases the ohmic resistance of the cell, which is why ESCs need to operate at temperatures above 1073 K to reach acceptable area specific resistances (ASR) [112]. This cell type is nonetheless attractive for commercial applications, e.g., Sunfire and BloomEnergy electrolyzer product portfolion, due to their excellent long-term and thermal cycling stability [113,114], reducing the maintenance cost of the electrolyzers. For instance, a 30-cell ESC stack operated at $-0.5\ \text{A cm}^{-2}$ and 1103 K for 4000 h shows a low degradation of $0.8\%\ \text{kh}^{-1}$ [115].

CSCs, whose mechanical stability is provided by a thicker cathode, show better electrochemical performance at the cost of long-term stability [116]. They reach higher current densities at significantly lower temperatures: Riedel et al. [112] were able to operate a 10 CSC stack at up to $-1.2\ \text{A cm}^{-2}$ at 1023 K, while a similar 10 ESC stack only reached $-0.7\ \text{A cm}^{-2}$ at 1073 K. With higher current densities, fewer cells are required to produce a given amount of hydrogen, leading to reduced CAPEX.

In order to capture the influence of all five SOEC operating parameters selected for the present optimization, the electrochemical behavior of the stack needs to be modeled with sufficient detail. To ensure that all relevant physical processes are taken into consideration, the multi-scale SOC stack simulation tool [81,82] which is part of the DETCHEM [117] software package was used.

The simulation software is built around a 1D+1D cell model that comprises a plug flow model for the gas channels, a dusty gas model for

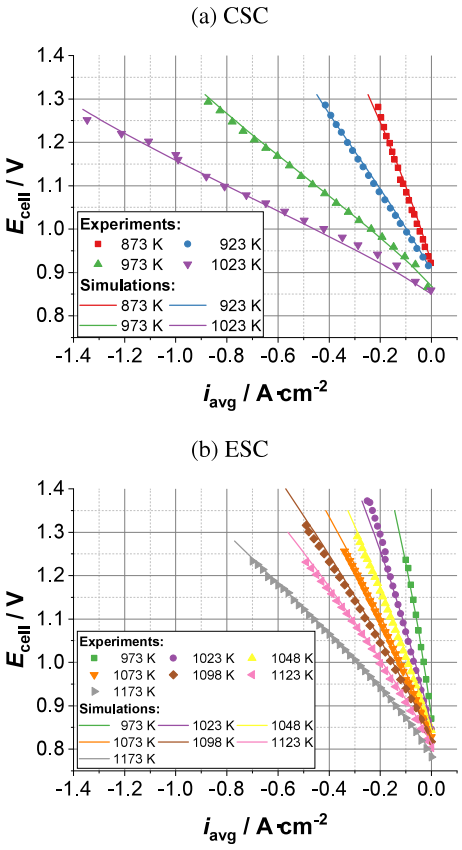

Fig. 9. Validation of the cell model via the measurement and simulation of steady-state polarization curves of 10.18 cm^2 cells for $p = 1$ atm, 9 : 1 H_2O to H_2 volume ratio, $\dot{V}_{\text{air,in}} = 114.5\ \text{N mL min}^{-1}$ and $\dot{V}_{\text{fuel,in}} = 76.6\ \text{N mL min}^{-1}$ (ESC)/$\dot{V}_{\text{fuel,in}} = 44.0–171.6\ \text{N mL min}^{-1}$ (CSC). Adapted from Wehrle et al. [82]. Copyright 2022, with permission from Elsevier.

mass transport in the electrodes, a distributed charge transport model across the electrodes and electrolyte, global Butler-Volmer kinetics for the electrochemical reactions and a 2D heat transport model for the solid phase. This cell model is then used by a stack model to simulate single repeating units (RU) in the SOEC stack [81,82].

Microstructural analysis and electrochemical characterization of the CSC (provided by the commercial supplier Elcogen) and the ESC (provided by the commercial supplier Kerafol) have been performed in a previous study by Wehrle et al. [82] in order to calibrate and validate the cell models. A comparison between planar cell experimental data and simulation results is provided in Fig. 9 and shows good agreement. Based on the experimentally validated single cell models, two (CSC- and ESC-) stack models were built, comprising 150 cells each with an active area of 128 cm^2 (9 cm × 14.2 cm). The stack was assumed to be insulated with a 5 cm layer of Promalight-1000X [118] and heat loss through free convection in ambient air at 298 K was considered.

In order to perform the PtM system simulations, the required stack model outputs are the average cell voltage E_{cell}, average gas temperature at the outlet $T_{\text{out}}^{\text{SOEC}}$ and maximum temperature gradient inside the stack ∇T_{max} as a function of the five optimization variables defined in Table 1. Thus, the in- and output interrelation can be summarized as Eqs. (5)–(7).

$$E_{\text{cell}} = f_1(i_{\text{stack}}, T_{\text{in}}^{\text{SOEC}}, p_{\text{in}}^{\text{SOEC}}, SC, \phi) \tag{5}$$

$$T_{\text{out}}^{\text{SOEC}} = f_2(i_{\text{stack}}, T_{\text{in}}^{\text{SOEC}}, p_{\text{in}}^{\text{SOEC}}, SC, \phi) \tag{6}$$

$$\nabla T_{\text{max}} = f_3(i_{\text{stack}}, T_{\text{in}}^{\text{SOEC}}, p_{\text{in}}^{\text{SOEC}}, SC, \phi) \tag{7}$$

The output of the SOEC stack model is used to calculate the electrical consumption of the stack and the heat demand or heat availability

Table 3
Varied parameters used to establish the performance maps of the SOEC stacks with a full factorial numerical experiment on the 3D stack models.

Parameter	Symbol	Unit	Values	
			CSC	ESC
Average current density	i_{stack}	A cm^{-2}	−0.3, −0.6, −0.9, −1.2, −1.5	−0.3, −0.6, −0.9, −1.2
Inlet gas temperature	T_{in}	K	923, 973, 1023	1073, 1123, 1173
Operating pressure	p	bar	1, 10, 20	1, 10, 20
Steam conversion	SC	%	70, 80, 90	70, 80, 90
Air-to-fuel ratio	ϕ	–	1, 3, 6	1, 3, 6

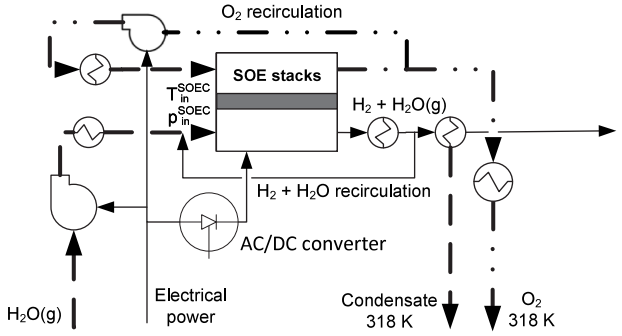

Fig. 10. Process diagram of the electrolysis units using oxygen as sweep gas.

generated by the gas flow at the output. Moreover, it is ensured that the temperature gradients inside the stack do not exceed 10 K cm^{-1} in order to limit degradation through thermal stress [119].

Since a large number of plant simulations have to be performed during an optimization, the long computation times of detailed stack simulations were circumvented by using simplified stack models implemented through multi-dimensional linear interpolation of detailed simulation results. The interpolation is performed on the results of a full factorial numerical experiment using the possible discrete variable values listed in Table 3, resulting in 1458 simulations and 3 multi-dimensional performance maps per combination of cell type and sweep gas.

The outputs of this reduced model are still functions of all the selected operating parameters, while the computation times are greatly reduced. The loss in accuracy depends on the amount of points computed, the interpolation method used and the behavior of the exact solutions to f_1, f_2 and f_3 in the region of interest. Since E_{cell} and T_{out}^{SOEC} are expected to be monotonous functions of the optimization variables inside the chosen domain [120–122], the linear interpolation method is expected to yield good approximations. However, ∇T_{max} is not a monotonous function of i_{stack} due to the transition between endothermic and exothermic operation, therefore the corresponding loss in accuracy is alleviated by the increased number of samples for the current density i_{stack}.

Ultimately, a very fast reduced stack model is obtained which accuracy is shown to be satisfactory in Section 3.1.

In the PtM plant, the electrolysis units includes multiple recirculation loops. The fuel (cathode) off-gas recycle loop regulates the inlet gas composition to 90% H_2O and 10% H_2, which is required to prevent re-oxidation of the nickel particles in the fuel electrode [123]. Thermal management of SOEC stack can be accomplished in multiple ways, including operation with air and pure oxygen as sweep gases. Feeding the stack with pure O_2 is achieved by implementing an anode off-gas recycle loop driven by a recycle blower, as depicted in Fig. 10. Full sweep gas recirculation (i) eliminates the need for sweep gas compression during pressurized operation, (ii) reduces the energy required to heat the sweep gas up to T_{in}^{SOEC} and (iii) produces pure O_2 as a byproduct, which is used in the BG unit for efficient N_2-lean syngas production [37].

For all other plant concepts, operation with air (without recirculation) is also simulated, since this simpler design better reflects the state-of-the-art.

The steam, sweep gas and recirculation blower work is computed using Eq. (8), which comprises the fan and electric motor efficiencies $\eta_{fan} = 0.8$ [124] and $\eta_{el} = 0.95$ [62], the required volumetric flow rate $\dot{V}_{blow}$ and the pressure drop Δp_{stack}.

$$P_{el,blow} = \eta_{fan} \cdot \eta_{el} \cdot \Delta p_{stack} \cdot \dot{V}_{blow} \quad (8)$$

The latter was obtained by implementing the manifold and stack flow model proposed by Koh et al. [125], which was further improved to take into account (i) the thermal volume expansion/contraction of the gases caused by temperature fluctuations across the stack and (ii) the density variation in the gas channels due to mass transport through the electrolyte.

Since a continuous current needs to be supplied to the SOEC stack, losses from a power inverter ($\eta_{AC/DC} = 96\%$) are also accounted for. The heat dissipated by the electric inverter is expected to be of low quality and is therefore not included in the pinch analysis.

2.2.4. Condensers and compressors

Because the operating pressure between system components can vary significantly, mechanical gas compression is needed at varying points in the plant. In order to reduce compression work, gases are cooled to 319 K (with condensation of excess steam) before each compression step. A maximal compression ratio of 6 was chosen, above which compression is performed in multiple steps with identical compression ratios and intermediate cooling. An isentropic compression efficiency of 75% and a mechanical efficiency of 90% was assumed in the adiabatic compressors [65]. All hot gas cooling duties resulting from compression processes are considered in the pinch analysis.

When condensation is required, e.g., downstream the methanation for product separation, the gases are cooled down to 319 K for water knock-out with a minimum allowed steam partial pressure of 0.1 bar. The cooling duties are also included in the pinch analysis.

In the SNG conditioning unit, the CH_4-rich product gas is condensed and then further dried to 50 mg N m^{-3} H_2O in a zeolite-based molecular sieve [126] (see *SNG conditioning unit* in Fig. 3) to comply with the DIN EN 16726 European standard for H-gas [86,104]. A minimal methane content of 95% and maximum hydrogen content of 2% is achieved through suitable selection of methanation process operating conditions. Finally, the SNG is compressed to 200 bar, which corresponds to the pressure used in European vehicles [87].

2.3. Optimization algorithm

The use of optimization algorithms enables a systematic, target-oriented and automatized determination of optimal operation conditions for all plant components. Specifically, setting up a systematic procedure largely facilitates the execution of a robust comparative energy assessment of different plant concepts without relying on guesses or intuition. Because some subsystems are simulated using complex external models, derivative-free constrained optimization algorithms are required.

Eight operation parameters were selected for optimization, five for the electrolyzer and three for the methanation unit (see Table 1). The

optimization was performed with the aim of maximizing the net PtM system efficiency with respect to the output HHV, as defined in Section 2.1. Additionally, the optimum was constrained by the maximum temperature gradient in the electrolyzer (10 K cm^{-1} [119]) and an SNG output suitable for use as an automotive fuel.

It was found that the solution space of the present optimization problem contains a large number of local optima, which makes the determination of the global optimum difficult. Although it is not possible to ensure that the global optimum of the optimization problem is found, the reliability of the results of the optimization methods was assessed by performing the optimizations multiple times (starting from random initial points for the deterministic optimization algorithms) while ensuring that the results are identical. A tolerance of 0.1% for the optima and 1% for the optimization variables is allowed in order to account for the convergence criterion of the optimization algorithm.

The PDFO optimizer suite [127–129] was first tested for the optimizations in this study, as it contains specialized tools for derivative-free constrained optimization. Unfortunately, the presence of local optima proved to be a hurdle for this method, as multiple optimizations started from random initial points of the parameter space yielded different optima. Therefore, the simulated annealing routine from the Matlab optimization toolbox was tested, as the algorithm is designed with the express purpose of global optimization in the presence of local optima. However, the optimizer settings required to reach reliable results led to very high computation times, with the number of computed data points approaching the millions. Recognizing that the local optima were reasonably distant from each other inspired the combination of Monte-Carlo and Nelder–Mead [130] algorithms ultimately used in this study, which allowed to reach reliable results with reasonable computation times.

The implemented method starts with a Monte Carlo optimization that samples random points in the parameter space. Such a stochastic optimization method converges toward the global optimum for an infinite number of samples, but sampling only 10 000 points was found to already provide good enough coverage of the parameter space to serve as a basis for a method that converges toward the closest local optimum. The Nelder–Mead algorithm is the gradient-free simplex optimization method chosen for this local optimization task. It was selected because it is a well-documented method that is easy to implement, and therefore to customize. The custom implementation made for this study uses the nine best (highest efficiency) sample points of the Monte-Carlo algorithm as starting points, and comprises an added penalty system that constrains the parameter space by rejecting invalid plant operating conditions. As the algorithm struggled to converge toward optima located directly at the limits of the parameter space, the Nelder–Mead algorithm was also modified to specifically consider points directly at the boundaries of the parameter space whenever the method converged toward them. The resulting algorithm converges in approximately 200 steps, resulting in a method that is much faster and, for this specific application, just as reliable as simulated annealing. The approximately 10 200 simulations required for an optimization resulted in single-core computation times of about 4 h for cases with 3PM reactors and 8 h for cases with FBM reactors. Simulations of FBM reactors are more computationally intensive because the gas composition at the inlet of the first reactor is computed iteratively due to the recirculation of the output of the first reactor. The memory requirement for these computations is minimal.

The final results reported in this study were obtained by performing each of the optimizations at least twice and never observing any significant change in the results. Although these results cannot be proven to be the global optima of the optimization problems, the flawless replication of over 50 optimizations, which always start from random samples, lends credibility to the assumption that the results represent the global optima.

Table 4
ASR of the CSC and ESC stacks for $i_{stack} = -0.3$ A cm^{-2}, $SC = 80\%$, $\phi = 1$ and fuel composition of 90% H_2O/10% H_2.

Case	CSC stack at 973 K	ESC stack at 1123 K
1 bar, O_2	0.283 Ω cm^2	0.408 Ω cm^2
1 bar, air	0.290 Ω cm^2	0.427 Ω cm^2
20 bar, O_2	0.220 Ω cm^2	0.381 Ω cm^2
20 bar, air	0.229 Ω cm^2	0.390 Ω cm^2

3. Results and discussion

3.1. SOEC stack performance maps

Exemplary slices from the interpolated performance maps of the ESC and CSC, operated with air and oxygen as sweep gases, are depicted in Fig. 11. The contour plots represent the average cell potential E_{cell} in the stack, which is inversely proportional to its electrical efficiency, as a function of the average current density i_{stack} and the gas inlet temperature T_{in}^{SOEC}. The depicted slices correspond to operation at constant inlet pressure $p_{in}^{SOEC} = 1$ bar, conversion rate $SC = 80\%$ and air-to-fuel ratio $\phi = 1$. Moreover, Fig. 12 shows simulated polarization curves for the two stack designs for $T_{in}^{SOEC} = 1023$ K (CSC)/$T_{in}^{SOEC} = 1173$ K (ESC) at $p_{in}^{SOEC} = 1$ bar and $p_{in}^{SOEC} = 20$ bar. Area-specific resistances (ASR) of both stack designs calculated at $i_{stack} = -0.3$ A cm^{-2} for varying sweep gases and absolute pressures are provided in Table 4.

As can be seen in Fig. 11, the electrical efficiency of the stack improves as the thermal energy input increases, whilst increasing current density at a fixed gas inlet temperature requires to supply a higher cell voltage due to the overpotential losses.

In the low current density regime ($i_{stack} = -0.3$ A cm^{-2}), a similar cell potential $E_{cell} \approx 1.23$ V results from the ESC stack at $T_{in}^{SOEC} = 1173$ K and the CSC stack at $T_{in}^{SOEC} = 1023$ K. Since the CSC stack is characterized by a lower ASR ($ASR_{CSC,1023\ K} = 0.290$ Ω cm^2 and $ASR_{ESC,1173\ K} = 0.427$ Ω cm^2 at 1 bar, see also Fig. 12), the performance of the ESC stack decreases further at higher current densities compared to the CSC stack. Accordingly, a higher cell potential $E_{cell} = 1.42$ V and higher inlet temperature $T_{in}^{SOEC} = 1173$ K have to be supplied to the ESC stack to match the current density $i_{stack} = 1.2$ A cm^{-2} of the CSC ($E_{cell} = 1.32$ V, $T_{in}^{SOEC} = 1023$ K).

Comparing air with oxygen as sweep gases for the stack, a slight reduction of the cell potential can be distinguished in case of air supply to the anode-side channels. The largest benefit can be observed for the ESC at high current density and low temperature, with a reduction of the cell potential of up to 20 mV.

For the selected set of operating conditions depicted in Fig. 12, the CSC achieves a lower electricity consumption than the ESC in a large part of the polarization regime. Only at very low current density and under atmospheric pressure, the ESC shows partially superior electrical efficiency than the CSC, which is due to the increased open circuit voltage (OCV) at higher temperatures. The ASR of the CSC is lower in all cases, despite a 150 K lower operating temperature. As numerically investigated by Wehrle et al. [82] and in congruence with the experimental results from Riedel et al. [112], the two cell types show an opposing behavior under pressurized operation: the efficiency of the ESC decreases under pressure, while the CSC is more efficient under pressure at higher current densities ($i_{stack} > 0.7$ A cm^{-2}) and less efficient at low current densities ($i_{stack} < 0.5$ A cm^{-2}). For both cell types, the OCV increases at higher pressures due to the pressure dependence of the Gibbs free energy of reaction [112,131]. However, the ASR generally decreases under increasing pressure, as can be observed in Table 4, which is due to the faster electrochemical kinetics and reactant density in the electrodes [82]. In the case of the CSC, in which the impact of activation and concentration overpotentials is more severe, the ASR improves significantly. For the cases listed in Table 4, pressurized operation reduces the ASR by approximately 21% for the CSC and only 8% for the ESC.

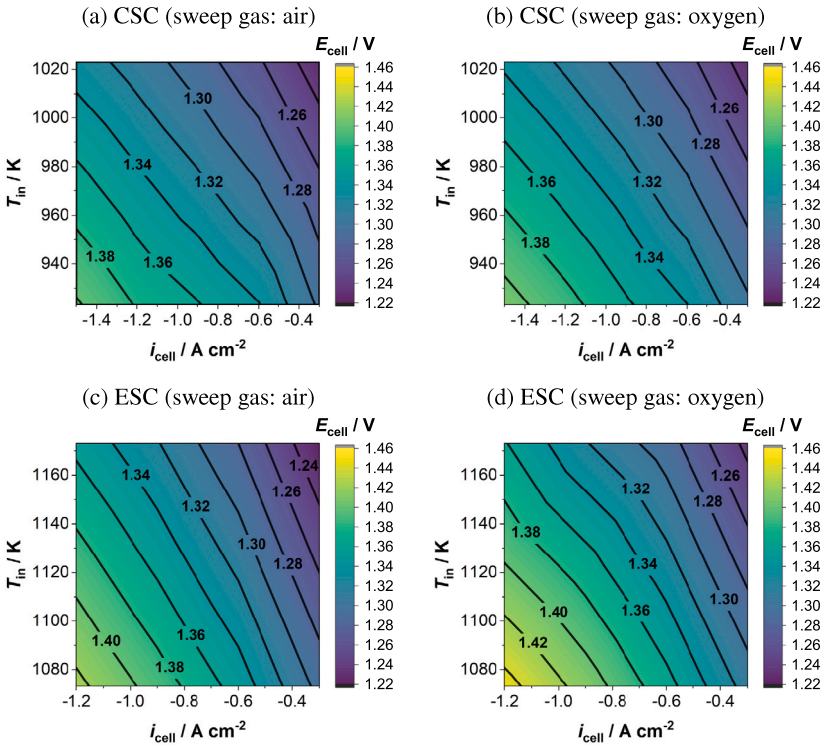

Fig. 11. Stack average cell potential as a function of gas inlet temperature and average current density for $p = 1$ bar, $SC = 80\%$, $\phi = 1$ and fuel composition of 90% H_2O/10% H_2.

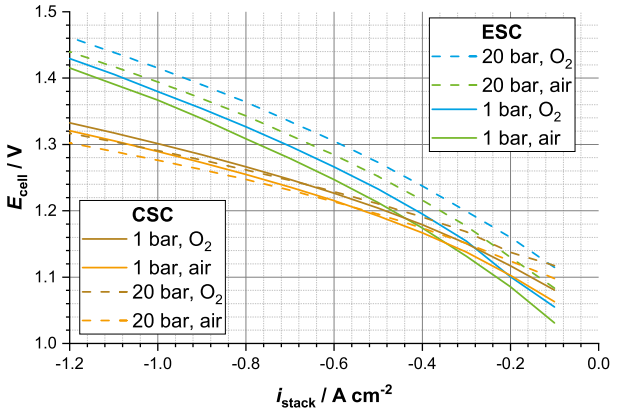

Fig. 12. Polarization curves of the CSC and ESC stacks for $SC = 80\%$, $\phi = 1$, $T_{in}^{SOEC} = 1023$ K (CSC)/$T_{in}^{SOEC} = 1173$ K (ESC) and fuel composition of 90% H_2O/10% H_2.

Table 5
Comparison of simulated and interpolated values for the air-fed CSC stack for $i_{stack} = -0.45$ A cm^{-2}, $p = 5$ bar, $T_{in}^{SOEC} = 998$ K, $SC = 75\%$ and $\phi = 2$.

Output	Unit	Simulated	Interpolated	Deviation
E_{cell}	V	1.267	1.248	1.5%
T_{out}	K	956.2	956.5	−0.031%
∇T_{max}	K cm^{-1}	5.31	4.89	7.9%

In order to estimate the accuracy of the interpolated values, an additional computation has been performed that does not correspond to a simulated point of the performance map (see Section 2.2.3). All the parameters for this simulation lie between discrete values listed in Table 3, which represents a worst-case scenario. The comparison between simulated and interpolated values is shown in Table 5 and the temperature profile of the simulated stack is depicted in Fig. 13.

While E_{cell} and T_{out} show excellent agreement, the highest deviation between simulated and interpolated values is found for ∇T_{max} with a relative deviation of 8%. Fortunately, the identified optimal process conditions (see Section 3.2) correspond to SOEC operation regimes with low temperature gradients, such that the limited accuracy in this value is not critical here.

3.2. Comparative assessment of PtM plant concepts

3.2.1. Plant concepts with oxygen-operated stacks

Table 6 lists the highest achievable PtM system efficiencies that can be reached for all plant concepts considering SOEC stacks operated with pure oxygen, alongside the respective operation parameters that minimize the system energy consumption. Fig. 14 depicts a cumulative bar chart representing the electricity consumers in the plants and their contribution to the total power requirement of the plant configurations for the production of 1 MW of SNG. A summary of the plant mass balances can be found in Appendix B, Table 12.

The CC process has the highest impact on the efficiency of the plant, with plants utilizing AGT and BG yielding higher efficiencies than DAC by approximately 10 pp.

Despite the selected BG process being autothermal, its thermal integration with the remaining plant is beneficial. In plants with BG, over 40% of the energy is provided by biomass, which significantly reduces the amount of electrolytic H_2 required. In optimized plants with both BG and CSC stacks, no electrical heating is required. Due to the lower number of SOECs required, the methanation heat is sufficient to evaporate and superheat the steam necessary for the gasification process and to operate the electrolyzer at lower steam conversion rates of $SC = 70\%$. In addition, the high temperature of the syngas stream exiting the gasification reactor ($T_{out}^{BG} = 1123$ K) can be used to heat up the SOEC inlet streams ($T_{in}^{SOEC} = 1023$ K), while the heat requirements of biomass drying and syngas cleaning can be fulfilled by lower temperature heat. When ESCs are used instead, a small amount of electrical heating is required between 1103 K and 1173 K due to their higher operating temperatures.

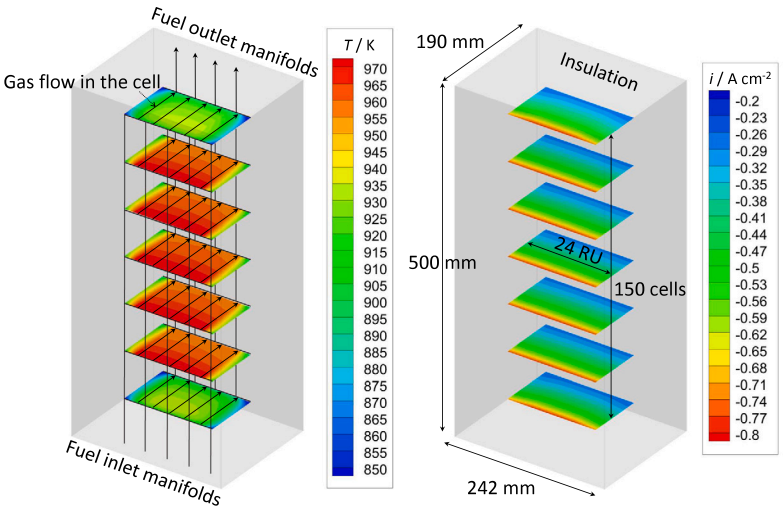

Fig. 13. Slices of the 3D solid phase temperature and current density distribution in the air-fed CSC stack active region for $i_{stack} = -0.45$ A cm^{-2}, $p = 5$ bar, $T_{in}^{SOEC} = 998$ K, $SC = 75\%$ and $\phi = 2$. The fuel gas flow, through the 5 inlet channels, 24 repeating units (RU) and 4 outlet channels is schematically depicted. Sweep gas flows in the same direction in a mirrored pattern (4 inlet channels, 5 outlet channels).

Table 6
Highest achievable efficiency and optimized operating conditions for every plant concept considered with oxygen-operated stacks.

Plant concept			Eff.	Stack					Methanation		
CO_2	Meth.	SOEC	η_{HHV} %	p bar	T_{in} K	$\lvert i_{stack}\rvert$ A cm^{-2}	SC %	ϕ –	p bar	T_{in} K	p_{cool} bar
BG	FBM	ESC	80.9	17.9	1173	0.300	70	6.0	19.9	523	21.8
		CSC	82.9	19.9	1023	0.300	70	6.0	19.9	523	21.1
	3PM	ESC	81.6	7.9	1173	0.300	70	6.0	10.0	525	20.4
		CSC	83.3	10.0	1023	0.300	70	6.0	10.0	526	17.4
AGT	FBM	ESC	81.2	4.4	1173	0.300	90	6.0	26.0	537	29.9
		CSC	81.5	5.1	1023	0.300	90	6.0	29.2	526	30.0
	3PM	ESC	84.3	2.6	1173	0.300	90	6.0	15.5	532	28.7
		CSC	84.6	19.2	1023	0.300	70	6.0	19.2	537	29.9
DAC	FBM	ESC	71.9	1.2	1173	0.300	90	6.0	27.7	535	29.9
		CSC	72.3	20.0	1023	0.300	70	6.0	21.0	523	29.9
	3PM	ESC	74.3	2.1	1173	0.300	90	6.0	12.4	531	29.4
		CSC	74.8	16.2	1023	0.300	70	6.0	16.4	549	29.7

BG: biomass gasification, AGT: amine gas treatment, DAC: direct air capture
FBM: fixed-bed methanation, 3PM: three-phase methanation
ESC: electrolyte-supported, cell CSC: cathode-supported cell.

Table 7
Highest achievable efficiency and optimized operating conditions for plant concepts with BG at 20 bar.

Plant concept			Eff.	Stack					Methanation		
CO_2	Meth.	SOEC	η_{HHV} %	p bar	T_{in} K	$\lvert i_{stack}\rvert$ A cm^{-2}	SC %	ϕ –	p bar	T_{in} K	p_{cool} bar
BG	FBM	ESC	84.9	20.0	1173	0.300	70	6.0	20.0	524	23.7
		CSC	86.8	20.0	1023	0.300	74	6.0	20.0	529	29.1
	3PM	ESC	84.9	20.0	1173	0.300	71	6.0	20.0	576	25.1
		CSC	87.0	20.0	1023	0.300	70	6.0	20.0	578	23.2

BG: biomass gasification, AGT: amine gas treatment, DAC: direct air capture
FBM: fixed-bed methanation, 3PM: three-phase methanation
ESC: electrolyte-supported, cell CSC: cathode-supported cell.

In order to investigate the system integration opportunities with pressurized BG, a set of optimizations was performed with the assumption that the BG process and the SOECs are both operated at 20 bar. Therefore, no O_2 compression is required. The results are depicted in Table 7. The corresponding mass balances can be found in Appendix B, Table 13.

Pressurized BG is highly beneficial, as the efficiencies achieved are superior by approximately 4 pp for all plant concepts. At 20 bar,

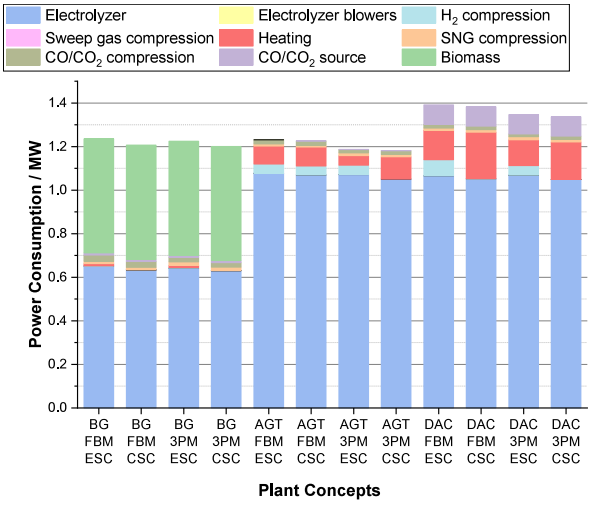

BG: biomass gasification, AGT: amine gas treatment, DAC: direct air capture, FBM: fixed-bed methanation, 3PM: three-phase methanation, ESC: electrolyte-supported, cell CSC: cathode-supported cell

Fig. 14. Breakdown of the power consumption of all sub-processes with oxygen-operated stacks for the production of 1 MW of SNG. BG: biomass gasification, AGT: amine gas treatment, DAC: direct air capture, FBM: fixed-bed methanation, 3PM: three-phase methanation, ESC: electrolyte-supported, cell CSC: cathode-supported cell.

the BG yields a much higher amount of CH_4 (16.7 vol% at 20 bar, 6.0 vol% at 1 bar) while the H_2, CO_2, CO yield drop from 35.4%, 25.5%, 21.9% at 1 bar to 28.7%, 34.0%, 18.6% at 20 bar respectively. As long as the electrolysis process is performed under pressure and with recirculated O_2 as sweep gas, pressurized BG is a net improvement, which is congruent with the observation of Anghilante et al. [37].

Plants using AGT as CC technology reach the highest efficiency. The heating duties of the CC process and H_2O evaporation are fully covered by the methanation reaction heat, while a moderate amount of electrical heating is required to heat up O_2 and steam to the SOEC inlet temperature. The power consumption of the sorbent pumps is also negligible.

Conversely, process integration of DAC increases the power consumption of the plant by up to 12% compared to the process using AGT (see Fig. 14). The majority of the power requirement of the DAC process is thermal [93,96,132], although approximately 10% of the

total plant power consumption is the electricity needed to operate the large amount of fans and vacuum pumps required for the process due to the low concentration of CO_2 in air (approximately 420 ppm [133]).

3PM yields the highest plant efficiencies in all presented cases. The reasons are twofold: (i) The product gas of the FBM is hotter, leading to a shift of the thermodynamic equilibrium toward the reactants which must be compensated with higher methanation pressures in order to reach the desired methane yield. Hence, the methanation pressure is higher in all plants including FBM reactors, leading to the increase in compression work most noticeable for the AGT plant concepts in Fig. 14. Conversely, operating the methanation units at the higher temperatures and pressures close to the SOEC leads to maximum system efficiency. (ii) Due to the higher reactant conversion, 3PM reactors produce larger amounts of heat at a lower temperature. In plant concepts with AGT or DAC, where a significant quantity of low temperature heat is needed, 3PM presents a significant advantage.

The discrepancy between both methanation processes is much smaller in plant concepts with BG because the gasification process increases the methane yield and reduces the heat requirement of the plant.

Under optimized conditions, the PtM system efficiency increases by up to 2.5% when using CSCs instead of ESCs due to the reduction of the electric power consumption of the stack. CSCs also perform well at elevated pressures, which is an advantageous mode of operation in plants using O_2 as sweep gas: pressurized operation of the SOEC reduces the total compression work required in the plant, since the output pressure of the produced H_2 matches the methanation reactor pressure more closely, and the O_2 does not need to be compressed due to the recirculation. While the maximum system efficiencies do not differ much between both cell types, the optimal operating pressure of the stack does depend on the cell design. While CSCs benefit from better performance at high pressures, ESCs should rather be operated at slightly lower pressures (see Table 6), which is a trade-off between H_2 compression work and stack performance.

The optimal steam conversion rate for a given plant configuration depends on the availability of surplus heat. For plants in which sufficient heat is available for water evaporation, operating the SOECs with a steam conversion of 70% decreases concentration overpotential losses and increases the plant efficiency (see Table 6). However, in plants with DAC and AGT units, the interactions are more complex, since the CSC are operated at lower steam conversion rates despite the need for additional heating. In these plants, the model indicates that the methanation heat is better utilized to reduce the concentration overpotential across the cells rather than minimizing electrical heating.

For every case, the optimal current density with respect to plant efficiency is at the lower boundary, $i_{stack} = -0.3\ A\,cm^{-2}$. Those conditions correspond to the endothermic operation regime at the upper boundary temperatures of 1173 K for the ESC and 1023 K for the CSC. The elevated oxygen-to-fuel ratio $\phi = 6$ maintains practical stack temperatures, which also keeps temperature gradients well below the defined limit of 10 $K\,cm^{-1}$. High gas temperatures improve the electrochemical performance of the SOECs by reducing the ASR. Endothermic, low current density operation maximizes the efficiency due to the reduction of overpotential losses and the utilization of thermal energy. Low current densities and high operating pressures also lead to lower volume flow through the stack, which minimizes blower work.

Although low current densities and high gas temperatures yield the highest plant efficiencies, these operating conditions raise CAPEX due to the higher number of SOEC stacks required to produce a given amount of SNG [134]. Further, operation at high temperatures leads to a cost enhancement of SOEC module and heating apparatus materials (interconnects, sealing, insulation, etc.) [135]. The preferred point of operation of SOEC stacks is the thermoneutral voltage because it simplifies the thermal management and system design [136]. Therefore, a similar set of optimizations was performed with electrolyzers operated under thermoneutral conditions, presented in Table 8.

Table 8
Highest achievable efficiency and optimized operating conditions for every plant concept considered with oxygen-operated stacks under thermoneutral conditions.

Plant concept			Eff.	Stack					Methanation		
CO_2	Meth.	SOEC	η_{HHV} %	p bar	T_{in} K	$\lvert i_{stack}\rvert$ A cm^{-2}	SC %	ϕ –	p bar	T_{in} K	p_{cool} bar
BG	FBM	ESC	77.9	19.9	1172	0.559	83	6.0	20.1	523	22.6
		CSC	78.4	20.0	1022	0.999	73	6.0	20.0	523	26.9
	3PM	ESC	78.1	10.0	1157	0.521	85	6.0	10.0	526	22.2
		CSC	78.6	10.0	1022	1.012	70	3.0	10.0	526	16.8
AGT	FBM	ESC	76.2	20.0	1169	0.525	90	6.0	23.7	532	30.0
		CSC	76.6	19.8	1018	0.838	90	4.4	22.7	528	29.7
	3PM	ESC	78.9	19.0	1173	0.545	90	6.0	19.0	555	30.0
		CSC	79.3	19.9	1019	0.852	90	3.9	19.9	552	29.7
DAC	FBM	ESC	68.0	19.8	1170	0.530	90	6.0	21.9	525	29.7
		CSC	68.3	20.0	1015	0.811	90	6.0	20.5	523	29.6
	3PM	ESC	70.1	19.4	1171	0.538	90	6.0	19.4	568	29.8
		CSC	70.4	18.6	1017	0.834	90	5.3	18.8	560	29.5

BG: biomass gasification, AGT: amine gas treatment, DAC: direct air capture
FBM: fixed-bed methanation, 3PM: three-phase methanation
ESC: electrolyte-supported, cell CSC: cathode-supported cell.

The average current density in the stack was selected such that the temperature T_{out}^{SOEC} of the gas output of the stack matches the temperature T_{in}^{SOEC} of the gas input, which yields average cell voltages $E_{cell,TNV}$ between 1.29 V and 1.3 V depending on the heat loss to the environment and the electric potential distribution along the height of the stack.

Enforcing thermoneutral operation causes a large reduction in achievable plant efficiency between 3 and 5 pp, which would lead to a significant increase in operating costs. In particular, plant concepts with AGT experience the largest efficiency loss since the additional heat production by the SOECs cannot be utilized as effectively as the plant concepts with DAC. The efficiency of plant concepts with BG does not change as much because of the lower amount of electrolytic H_2 produced.

As can be extracted from Table 8, under optimized conditions, CSCs reach distinctly higher current densities ($\Delta i_{stack} \approx 50\%–90\%$) at thermoneutral conditions compared to ESCs whilst operating at lower temperatures ($\Delta T_{stack} \approx 130–150$ K). In the present cases, the superior electrochemical performance of the CSC is amplified by the pressurized operating conditions leading to highest system efficiencies, similarly to the previous results.

Additionally, thermoneutral SOEC operations allows for lower air-to-fuel ratios, which enables the operation of the SOECs at slightly higher pressures in the AGT plant concepts due to the reduction of the sweep gas compression work.

3.2.2. Plant concepts with air-operated stacks

Table 9 and Fig. 15 deliver a similar overview of the results as in the previous section, but for process chains in which air is used as SOEC sweep gas instead of pure oxygen. Since oxygen is required to operate the selected biomass gasification technology, the plant concepts in this section are limited to AGT and DAC as CC technologies. A summary of the plant mass balances can be found in Appendix B, Table 14.

Despite the slight improvement in stack performance when air is used as sweep gas, as noted in Section 3.1, the absence of a sweep gas recirculation loop causes a major system performance reduction, as seen in Table 9 and shown by Wang et al. [38]. PtM efficiencies are approximately 5 pp lower for plants with AGT and approximately 4 pp lower for plants with DAC. This represents an increase of the energy consumption of up to 6.8% in the AGT 3PM ESC process chain.

Contrary to the first case, the highest efficiencies are achieved with stacks operated at atmospheric pressure, as the sweep gas compression work performed during pressurized operation with air outweighs the savings of H_2 compression work. This is congruent with the finding of

Table 9
Highest achievable efficiency and optimized operating conditions for every plant concept considered with air-operated stacks.

Plant concept			Eff.	Stack					Methanation		
CO_2	Meth.	SOEC	η_{HHV} %	p bar	T_{in} K	$\lvert i_{stack}\rvert$ A cm^{-2}	SC %	ϕ –	p bar	T_{in} K	p_{cool} bar
AGT	FBM	ESC	76.6	1.0	1172	0.300	90	3.0	29.9	533	29.4
		CSC	76.5	1.0	1023	0.300	90	3.0	29.9	531	29.6
	3PM	ESC	79.0	1.0	1173	0.300	90	3.0	29.2	590	29.8
		CSC	79.0	1.0	1023	0.302	90	3.0	28.8	581	29.8
DAC	FBM	ESC	68.2	1.0	1173	0.300	90	2.8	30.0	534	29.9
		CSC	68.2	1.0	1023	0.300	90	3.0	29.8	531	29.3
	3PM	ESC	70.2	1.0	1173	0.302	90	3.0	23.1	582	29.4
		CSC	70.2	1.0	1023	0.300	90	3.0	24.9	588	29.8

BG: biomass gasification, AGT: amine gas treatment, DAC: direct air capture
FBM: fixed-bed methanation, 3PM: three-phase methanation
ESC: electrolyte-supported, cell CSC: cathode-supported cell.

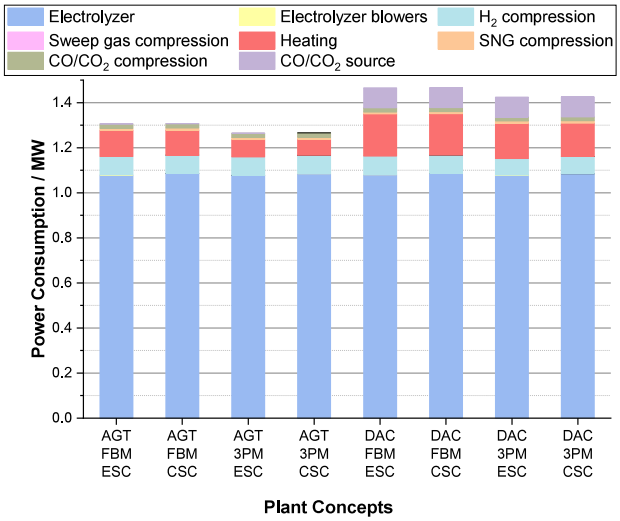

Fig. 15. Breakdown of the power consumption of all sub-processes with air-operated stacks for the production of 1 MW of SNG. BG: biomass gasification, AGT: amine gas treatment, DAC: direct air capture, FBM: fixed-bed methanation, 3PM: three-phase methanation, ESC: electrolyte-supported, cell CSC: cathode-supported cell.

Wehrle et al. [82]. With the reduced operating pressure, no difference between the efficiencies reached with CSCs and ESCs is observed. Although the electrical power consumption of ESCs is marginally lower than CSCs at −0.3 A cm^{-2}, their higher operating temperatures lead to a slight increase in heating requirements.

Due to the absence of sweep gas recirculation, additional heat is required to heat up air from the ambient temperature to T_{in}^{SOEC}, which cannot be fully covered by heat exchangers at the electrolyzer output. Therefore, lower air-to-fuel ratios of $\phi \approx 3$ are optimal in most cases, although the operating conditions are still endothermic. This additional heat requirement is also the reason why higher steam conversions of $SC \approx 90$ percent are required.

Compared to the previous section, the optimal methanation pressure is lower for all plant concepts. While reducing the compression work at the cost of a less favorable thermodynamic equilibrium is a worthwhile design choice in the first case, these plant concepts can utilize the low temperature heat generated during the compression, making higher methanation pressures more attractive.

A similar set of optimizations was performed with electrolyzers operated under thermoneutral conditions, presented in Table 10.

Table 10
Highest achievable efficiency and optimized operating conditions for every plant concept considered with air-operated stacks under thermoneutral conditions.

Plant concept			Eff.	Stack					Methanation		
CO_2	Meth.	SOEC	η_{HHV} %	p bar	T_{in} K	$\lvert i_{stack}\rvert$ A cm^{-2}	SC %	ϕ –	p bar	T_{in} K	p_{cool} bar
AGT	FBM	ESC	75.3	1.0	1173	0.715	90	1.0	29.2	533	29.7
		CSC	75.4	1.0	1023	0.868	90	1.0	29.5	531	29.7
	3PM	ESC	77.7	1.0	1173	0.716	90	1.1	26.1	570	30.0
		CSC	77.8	1.0	1021	0.857	90	1.0	26.0	572	29.4
DAC	FBM	ESC	67.2	1.0	1172	0.711	90	1.0	29.1	537	29.8
		CSC	67.3	1.0	1023	0.867	90	1.0	26.8	540	29.6
	3PM	ESC	69.1	1.0	1173	0.714	90	1.0	21.0	546	29.7
		CSC	69.3	1.0	1020	0.851	90	1.0	21.7	571	29.6

BG: biomass gasification, AGT: amine gas treatment, DAC: direct air capture
FBM: fixed-bed methanation, 3PM: three-phase methanation
ESC: electrolyte-supported, cell CSC: cathode-supported cell.

Table 11
Highest achievable efficiency for every plant concept considered with and without thermal integration of the CC process into the PtM plant.

	Plant concept			CC integration	
	CO_2	Meth.	SOEC	Yes	No
				η_{HHV} %	η_{HHV} %
Sweep gas: Oxygen	BG	FBM	ESC	80.9	80.7
			CSC	82.9	81.6
		3PM	ESC	81.6	81.3
			CSC	**83.6**	**82.0**
	AGT	FBM	ESC	81.2	75.9
			CSC	81.5	76.9
		3PM	ESC	**84.3**	**76.9**
			CSC	84.6	78.1
	DAC	FBM	ESC	71.9	67.3
			CSC	72.3	67.8
		3PM	ESC	74.3	68.2
			CSC	74.8	69.0
Sweep gas: Air	AGT	FBM	ESC	76.6	70.3
			CSC	76.5	70.0
		3PM	ESC	**79.0**	**70.8**
			CSC	79.0	70.9
	DAC	FBM	ESC	68.2	62.4
			CSC	68.2	62.4
		3PM	ESC	**70.2**	**63.3**
			CSC	**70.2**	**63.3**

BG: biomass gasification, AGT: amine gas treatment, DAC: direct air capture, FBM: fixed-bed methanation, 3PM: three-phase methanation, ESC: electrolyte-supported, cell CSC: cathode-supported cell, CC: carbon capture.

As opposed to the process chains compared in Section 3.2.1, the efficiency of the present plant concepts with thermoneutral SOEC operation (Table 9) is close to the efficiency of the same plant concepts with endothermic operation (Table 10), with a difference of up to 1 pp. This can be attributed to the higher heat requirement of these plant concepts, as illustrated in Fig. 15, in which the additional heat produced by the SOECs reduces the amount of additional electric heating required in the plant.

3.3. Comparison with PtM plants without CC integration

To evaluate the efficiency gain provided by thermal integration of CC technologies into the PtM process chains, the optimizations of the plant concepts presented in Sections 3.2.1 and 3.2.2 were repeated while thermally integrating the CC process and the remaining PtM process separately, thereby computing the efficiency of a system comprising a standalone CC plant delivering syngas or CO_2 to a PtM plant. In process chains with BG, the SOEC is still assumed to deliver O_2 to the process. The results are listed in Table 11.

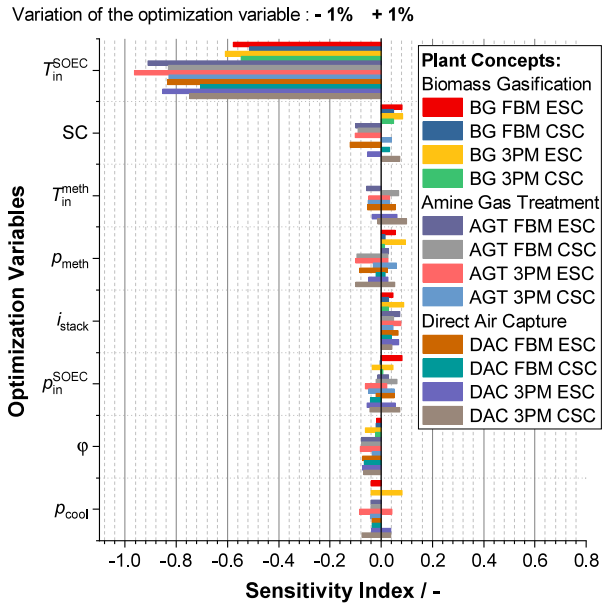

Fig. 16. Tornado diagram of the impact of a variation of the optimization variables on the efficiency of plant concepts using oxygen-operated stacks. BG: biomass gasification, AGT: amine gas treatment, DAC: direct air capture, FBM: fixed-bed methanation, 3PM: three-phase methanation, ESC: electrolyte-supported, cell CSC: cathode-supported cell.

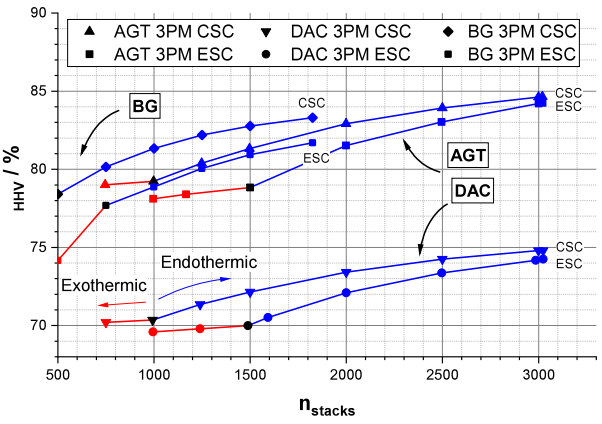

Fig. 17. Pareto front of plant efficiency and number of SOEC stacks in 20 MW_{SNG} BG 3PM, AGT 3PM and DAC 3PM plant concepts for ESCs and CSCs with O_2 sweep. BG: biomass gasification, AGT: amine gas treatment, DAC: direct air capture, 3PM: three-phase methanation, ESC: electrolyte-supported, cell CSC: cathode-supported cell.

Separating the two processes has a small impact on the efficiency of the BG process chains, with the largest efficiency loss being 1.6 pp in the BG 3PM CSC plant concept. This is easily explained by the fact that the BG process is autothermal, so that thermal integration of this process into the PtM plant mainly serves to recuperate moderate amounts of high-temperature heat in order to superheat steam above the temperature provided by the methanation process. However, the main advantage of the integration of the BG process into PtM plants is that the oxygen produced as a byproduct of the electrolysis process is utilized.

Conversely, the DAC and AGT processes benefit greatly from their thermal integration into PtM plants, which raises their respective total efficiencies by as much as 10.9% and 10.4%. Since these CC processes require large amounts of heat for the desorption of CO_2, they utilize the surplus of heat produced by the methanation process effectively.

3.4. Sensitivity analysis

In order to quantitatively assess the influence of the optimization variables on the plant efficiency, a sensitivity analysis was performed on every plant concept examined in Section 3.2.1. The optimized plant configurations were used as baseline while each optimization variable was increased and reduced by 1% to compute a sensitivity index SI according to Eq. (9).

$$\mathrm{SI} = -\frac{\Delta\eta_{\mathrm{HHV}}/\eta_{\mathrm{HHV}}}{\Delta P_i/P_i} \tag{9}$$

η_{HHV} is the efficiency of the optimized plant, while $\Delta\eta_{\mathrm{HHV}}$ is the change in efficiency when the parameter i of value P is varied by ΔP. Since $\Delta\eta_{\mathrm{HHV}}$ is always negative, SI is defined so that it is positive for an increase of P and negative for a decrease of P. The results of this analysis are depicted in Fig. 16.

Because some variables have their optimal values at the edge of the range defined in Table 1, variations that would exceed this range or invalidate the constraints of the optimization (CH_4 and H_2 content, $\nabla T_{\max}$) were not performed. In cases where the SOEC pressure $p_{\mathrm{in}}^{\mathrm{SOEC}}$ would exceed the methanation pressure $p_{\mathrm{in}}^{\mathrm{meth}}$, both variables are varied simultaneously.

For every plant concept, lowering the stack inlet temperature $T_{\mathrm{in}}^{\mathrm{SOEC}}$ has the largest impact on the plant efficiency. This is related to the assumption that high temperature heat can be produced electrically at 100% efficiency [37,65], making it advantageous to supply the SOEC with higher amounts of thermal energy instead of electrical energy, which would lead to higher electric inverter losses. However, the plant efficiency has a much lower sensitivity to the current density i_{stack}, which correlates directly with the electrical energy supplied to the stack. In other words, the stack efficiency is more sensible to changes in temperature than to changes in current density. Therefore, it can be deduced that the observed sensitivity is rather a result of the increased electrochemical performance of the SOEC at elevated temperatures, where the ASR is reduced.

The sensitivity of the plant efficiency relative to the remaining optimization variables is approximately equal. In agreement with the literature [24,64], the efficiency loss observed when increasing the steam conversion SC (which leads to slight reductions in the performance of the SOECs), is of similar magnitude than the loss observed when reducing the steam conversion SC (which increases the amount of superheated steam required). This trend showcases that the efficiency of SOEC systems can be improved using residual low-temperature heat to evaporate water.

3.5. Bi-objective optimization of the plant efficiency and number of SOEC stacks

The previous sections focused entirely on maximizing the system efficiency, i.e. minimizing the electrical energy requirement (an therefore reducing OPEX) of the selected plant concepts. However, CAPEX are still a relevant part of the SNG production costs, and the capital investment is dominated by the SOEC stacks [104,134] and the CC system [137,138]. Therefore, a bi-objective optimization of the achievable efficiency and the minimal number of installed SOEC stacks for the production of 20 MW of SNG is performed and the resulting Pareto fronts are depicted in Fig. 17.

In all of the depicted plant concepts, CSCs permit to reach higher efficiencies than ESCs and can attain equivalent plant efficiencies while

reducing the amount of SOEC stacks required by up to 35% in low current density regions and 50% in high current density regions.

The use of CSCs increasingly benefits the plant efficiency when the number of stacks is reduced toward the thermoneutral point of CSCs (1000 stacks in plants with AGT and DAC, 500 stacks in the plant with BG), which corresponds to current densities of approximately $i_{stack} \approx -0.6\ A\,cm^{-2}$. Beyond this current density, endothermic operation of the CSC is not possible within the given constraints which leads to a change in slope. For ESCs, similar behavior is observed at current densities of approximately $i_{stack} \approx -0.9\ A\,cm^{-2}$.

In plants with DAC the excess heat generated by the exothermic electrolysis can be utilized effectively, leading to a plateau of $\eta_{HHV} \approx 70\%$ between thermoneutral and highly exothermic operation where the efficiency decreases by less than 0.5%. The same phenomenon is observed in the plants with AGT, with the plant efficiency dropping by no more than 1 pp while reducing the number of stacks by 33%. In plants with BG, exothermic operation leads to more significant losses due to the production of excess heat which cannot be utilized. Since the BG 3PM ESC process chain does not require a significant amount of electrical heating, the plant efficiency drops further as the SOEC performance degrades under inefficient operating conditions.

The observed trend demonstrates that in systems that can utilize heat effectively, exothermic operation of the SOECs can allow a significant reduction of the required number of stacks without significant increase of energy consumption compared to thermoneutral operation. The reduced number of stacks is expected to result in a reduction in plant CAPEX, as the only plant components that need to be adapted to the modified operating conditions are the heat exchangers at the SOEC gas outlets.

3.6. Comparison of results with existing literature

In order to validate the results of this study, the PtM efficiencies computed herein are compared to results of similar system simulation studies.

Wang et al. [64] report achieving energy efficiencies of up to 85.2% HHV in a PtM system comprising an isothermal methanation reactor ($p_{in}^{meth} = 26$ bar, $T_{in}^{meth} = 563$ K) and CSC stack ($i_{cell} = 0.34\ A\,cm^{-2}$, $p_{in}^{SOEC} = 26$ bar, $T_{in}^{SOEC} = 973$ K, $SC = 80\%$). The similar AGT 3PM CSC (air sweep) process, which was treated in Section 3.2.2, was shown to be 79.0% HHV efficient. Although this plant concept includes an AGT process, which reduces the plant efficiency significantly, the difference in efficiency of 7.3% (6.2 pp) is expected to be caused in equal measure by the power inverter losses of 4% which are accounted for in this study.

Anghilante et al. [37] compute efficiencies for three PtM plants with integrated BG. The most similar plant concept to this study is comprised of CSC stacks under thermoneutral conditions, a pressurized BG process and a methanation process comprising a 3PM reactor and a honeycomb reactor. A HHV efficiency of 81% is reported. For the comparison of results, a system simulation was performed using the BG 3PM CSC process chain with thermoneutral operation of the SOEC and the following operating conditions, which match the ones used in the Ref. [37]: $T_{in}^{SOEC} = 1023$ K, $p_{in}^{SOEC} = 20$ bar, $SC = 80\%$, $\phi = 1$, $T_{in}^{meth} = 563$ K, $p_{in}^{meth} = 20$ bar, $p_{cool} = 20$ bar. An efficiency of 82.2% is obtained. The difference can be attributed to the higher performance of the CSC in this study, which achieves a current density of $-0.958\ A\,cm^{-2}$ as compared to the $-0.8\ A\,cm^{-2}$ of the Ref. [37] at lower gas inlet temperatures (1023 K compared to 1073 K) under thermoneutral conditions. The pinch diagram produced by Anghilante et al. is compared to the process chain simulated herein in Fig. 18.

The differences in the hot stream and cold stream composite curves are due to (i) the lower temperature of the first 3PM reactor considered in this study, which results in a higher carbon utilization of 99.6% (as opposed to 97.8%) and hence a higher heat production, (ii) the honeycomb methanation process, which is not isothermal and hence results in a different slope of the hot stream composite curve before the isothermal methanation threshold and (iii) the difference in SOEC inlet temperature.

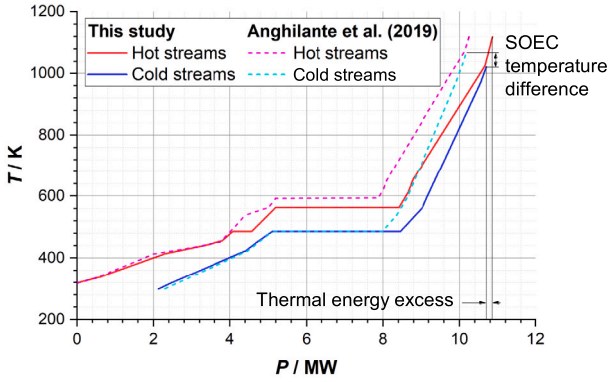

Fig. 18. Pinch diagram with the composite curves reported by Anghilante et al. compared to the similar system computed herein. Adapted from Anghilante et al. [37]. Copyright 2019, with permission from Elsevier.

The only published data on energy efficiency of PtM plants with integrated DAC process stems from Coppitters et al. [78,139], which report a HHV energy efficiency of up to 59.5% for a system including PEM electrolyzers and a series of four adiabatic methanation reactors. Process chains with DAC units and adiabatic methanation reactors simulated herein reached HHV efficiencies ranging between 67.2% and 72.3%. The difference in efficiency is mostly due to the superior performance of SOEC, as the PEM electrolyzers are reported to constitute 93% of the power consumption of the PtM system, as opposed to approximately 77% in the similar plants considered in this study.

Even though a study considering a PtM system with integrated AGT process can be found in the literature [79], it is specific to the integration in steelmaking plants. Therefore, no direct quantitative comparison can be made to the results produced herein.

4. Conclusion

A methodology for optimizing the operating conditions of PtM plants was presented and used to comparatively assess 20 different PtM plant concepts producing SNG suitable for use as a fuel.

A multi-scale SOEC stack model was used to compare the performance of an ESC stack and a CSC stack integrated into PtM plants. Operation with two sweep gas concepts, air and pure oxygen, was considered for both stack types. Fast SOEC stack models were build from simulated performance maps of detailed 3D models (provided in the Supplementary Information). The reduced models were integrated in the system simulations and shown to lead to a small loss in accuracy compared to the full models. Furthermore, the computed system efficiencies represent an upper limit, as the thermal integration through pinch analysis does not account for heat exchanger layout and heat loss through pipes.

The system simulation results indicate that with proper thermal integration, plants using BG and AGT as CO_2 sources can reach excellent HHV efficiencies of up to 87.0% and 84.6%, respectively, while plants with DAC units achieved up to 74.8% HHV efficiency. Sweep gas recirculation was shown to increase plant efficiency by up to 6.8%, both by reducing the amount of heating required and by allowing the advantageous pressurized operation of CSCs without the need for sweep gas compression. Thermal integration of the DAC and AGT processes into PtM plants was demonstrated to increase the efficiency of the complete system by a large margin of up to 10.9% and 10.4% respectively.

Endothermic SOEC stack operation leads to the highest PtM efficiencies due to reduced overpotential losses at low current densities,

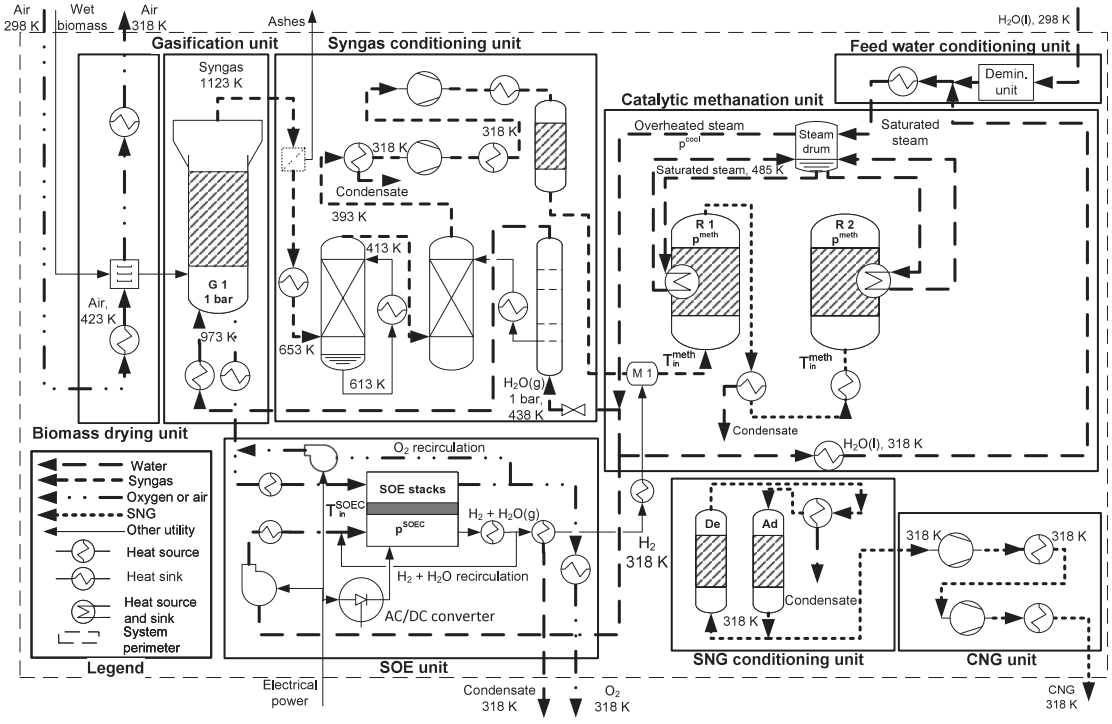

Fig. 19. PtM plant concept with BG, 3PM and sweep gas recirculation.

increased electrochemical performance at high gas temperatures, and reduced power inverter losses. Achievable system efficiencies with CSC and ESC stacks do not differ significantly, despite large differences in operating temperature ranges.

However, a Pareto optimization revealed that PtM plants with CSCs can achieve the same efficiency as plants with ESCs with half the number of SOEC stacks. Systems that effectively utilize heat were shown to benefit from a reduction in CAPEX with exothermic SOEC operation, while incurring an efficiency loss of less than 1% compared to thermoneutral operation. Considering the delicate balance between power density and degradation rate required for the commercially viable operation of SOECs, this observation warrants further investigation by means of techno-economic analysis.

The presented methodology provides valuable insights into synergistic process interactions that can be exploited to improve the system efficiency of PtM plant concepts. In particular, pressurized operation of ESC stacks resulted in higher PtM efficiencies, which is suboptimal for stand-alone operation, but advantageous at plant scale.

These results underline the significance of the present modeling and optimization approach for the design of thermally integrated PtM processes. Clearly, the methodological combination of optimization, pinch analysis and process modeling is a very powerful tool that can be easily adapted to other Power-to-X concepts.

CRediT authorship contribution statement

Oscar Furst: Writing – original draft, Validation, Software, Methodology, Investigation. **Lukas Wehrle:** Writing – review & editing, Software, Conceptualization. **Daniel Schmider:** Writing – review & editing. **Julian Dailly:** Resources. **Olaf Deutschmann:** Writing – review & editing, Supervision, Software, Funding acquisition, Conceptualization.

Declaration of competing interest

The authors declare that they have no known competing financial interests or personal relationships that could have appeared to influence the work reported in this paper.

Data availability

Data will be made available on request.

Acknowledgments

Funding

This work was supported by the German federal ministry for economic affairs and energy (Bundesministerium für Wirtschaft und Energie, BMWi) [grant numbers 03EIV041D, 03EIV041E] in the "MethFuel" group of the collaborative research project "MethQuest". The authors acknowledge support by the state of Baden-Württembergthrough bwHPC.

Omegadot software and consulting GmbH is gratefully acknowledged for a cost-free academic license of DETCHEM.

Parts of this work have been presented at the 18th International Symposium on Solid Oxide Fuel Cells in Boston, May 28–June 2 2023 [140].

Appendix A. Full plant process diagrams

See Figs. 19 and 20.

Appendix B. System mass balance tables

See Tables 12–14.

Appendix C. Supplementary data

The performance maps of the ESC and CSC stacks, for both air and oxygen as sweep gas, are provided as supplementary tables.

Supplementary material related to this article can be found online at https://doi.org/10.1016/j.apenergy.2024.123972.

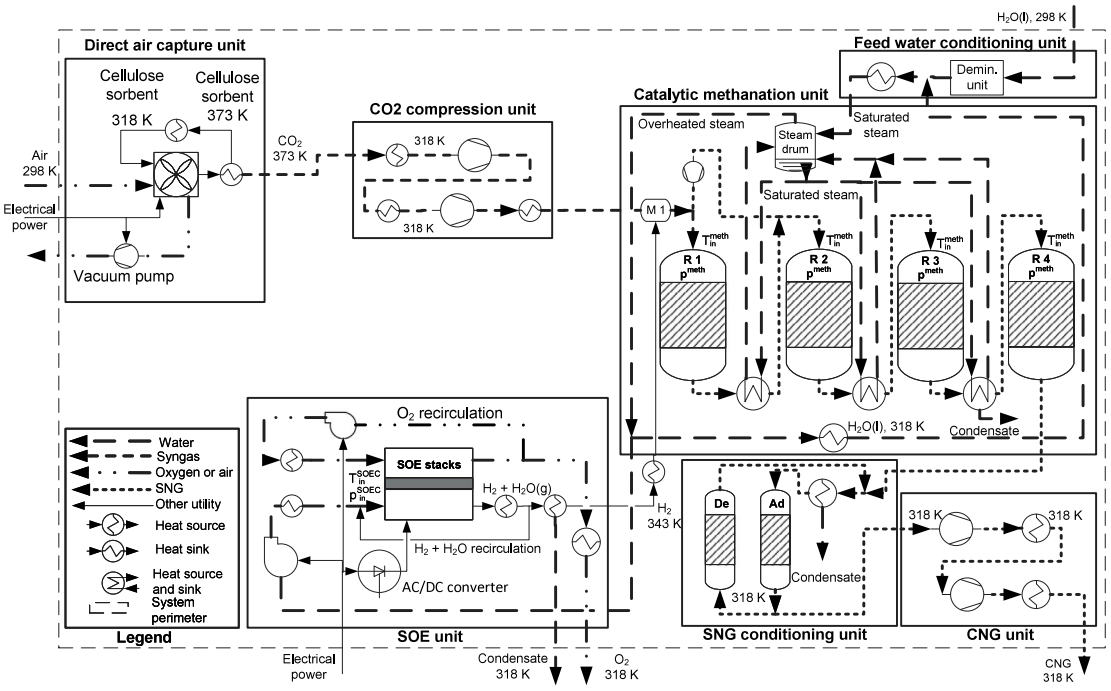

Fig. 20. PtM plant concept with DAC, FBM and sweep gas recirculation.

Table 12
Main mass streams at the inlet and outlet of the CC, SOEC and methanation units for every optimized plant concept considered with oxygen-operated stacks.

Plant concept			Carbon capture			SOEC				Methanation				
CO_2	Meth.	SOEC	$\dot{m}^{in}_{Bio.}$	$\dot{m}^{out}_{CO_2}$	$\dot{m}^{out}_{H_2O}$	$\dot{m}^{in}_{H_2O}$	$\dot{m}^{out}_{H_2}$	$\dot{m}^{out}_{H_2O}$	$\dot{m}^{out}_{O_2}$	$\dot{m}^{out}_{CH_4}$	$\dot{m}^{out}_{H_2O}$	$\dot{m}^{out}_{CO_2}$	$\dot{m}^{out}_{H_2}$	$\dot{m}^{out}_{C_2H_4}$
BG	FBM	ESC	0.569	0.454	0.073	1.346	0.110	0.363	0.702	0.360	0.252	0.006	0.001	0.000
		CSC	0.569	0.454	0.073	1.346	0.110	0.363	0.702	0.360	0.252	0.006	0.001	0.000
	3PM	ESC	0.568	0.453	0.073	1.344	0.110	0.363	0.701	0.360	0.241	0.005	0.001	0.000
		CSC	0.568	0.453	0.073	1.344	0.110	0.363	0.701	0.360	0.241	0.005	0.001	0.000
AGT	FBM	ESC	–	0.994	0.045	1.792	0.182	0.163	1.446	0.360	0.175	0.006	0.001	0.000
		CSC	–	0.993	0.045	1.789	0.182	0.164	1.444	0.360	0.146	0.004	0.001	0.000
	3PM	ESC	–	0.992	0.045	1.790	0.182	0.165	1.443	0.360	0.134	0.003	0.001	0.000
		CSC	–	0.991	0.045	2.224	0.182	0.601	1.442	0.360	0.104	0.003	0.001	0.000
DAC	FBM	ESC	–	0.994	0.002	1.790	0.182	0.163	1.446	0.360	0.160	0.005	0.001	0.000
		CSC	–	0.994	0.002	2.226	0.182	0.598	1.446	0.360	0.232	0.006	0.001	0.000
	3PM	ESC	–	0.993	0.002	1.788	0.182	0.162	1.444	0.360	0.180	0.004	0.001	0.000
		CSC	–	0.993	0.002	2.226	0.182	0.600	1.444	0.360	0.128	0.004	0.001	0.000

Table 13
Main mass streams at the inlet and outlet of the CC, SOEC and methanation units for every optimized plant concept considered with oxygen-operated stacks and 20 bar gasification.

Plant concept			Carbon capture			SOEC				Methanation				
CO_2	Meth.	SOEC	$\dot{m}^{in}_{Bio.}$	$\dot{m}^{out}_{CO_2}$	$\dot{m}^{out}_{H_2O}$	$\dot{m}^{in}_{H_2O}$	$\dot{m}^{out}_{H_2}$	$\dot{m}^{out}_{H_2O}$	$\dot{m}^{out}_{O_2}$	$\dot{m}^{out}_{CH_4}$	$\dot{m}^{out}_{H_2O}$	$\dot{m}^{out}_{CO_2}$	$\dot{m}^{out}_{H_2}$	$\dot{m}^{out}_{C_2H_4}$
BG	FBM	ESC	0.569	0.468	0.003	1.281	0.105	0.346	0.701	0.360	0.242	0.005	0.001	0.000
		CSC	0.569	0.468	0.003	1.226	0.105	0.290	0.702	0.360	0.244	0.006	0.001	0.000
	3PM	ESC	0.568	0.467	0.003	1.270	0.105	0.335	0.701	0.360	0.099	0.005	0.001	0.000
		CSC	0.568	0.468	0.003	1.281	0.105	0.346	0.701	0.360	0.100	0.005	0.001	0.000

Table 14
Main mass streams at the inlet and outlet of the CC, SOEC and methanation units for every optimized plant concept considered with air-operated stacks.

Plant concept			Carbon capture		SOEC				Methanation				
CO_2	Meth.	SOEC	$\dot{m}^{out}_{CO_2}$	$\dot{m}^{out}_{H_2O}$	$\dot{m}^{in}_{H_2O}$	$\dot{m}^{out}_{H_2}$	$\dot{m}^{out}_{H_2O}$	$\dot{m}^{out}_{O_2}$	$\dot{m}^{out}_{CH_4}$	$\dot{m}^{out}_{H_2O}$	$\dot{m}^{out}_{CO_2}$	$\dot{m}^{out}_{H_2}$	$\dot{m}^{out}_{C_2H_4}$
AGT	FBM	ESC	0.993	0.045	1.788	0.182	0.161	3.686	0.360	0.144	0.005	0.001	0.000
		CSC	0.993	0.045	1.788	0.182	0.162	3.676	0.360	0.144	0.004	0.001	0.000
	3PM	ESC	0.993	0.045	1.789	0.182	0.163	3.689	0.360	0.072	0.004	0.001	0.000
		CSC	0.992	0.045	1.788	0.182	0.162	3.690	0.360	0.071	0.004	0.001	0.000
DAC	FBM	ESC	0.993	0.002	1.788	0.182	0.161	3.542	0.360	0.144	0.005	0.001	0.000
		CSC	0.993	0.002	1.787	0.182	0.161	3.691	0.360	0.144	0.005	0.001	0.000
	3PM	ESC	0.993	0.002	1.788	0.182	0.161	3.692	0.360	0.090	0.005	0.001	0.000
		CSC	0.993	0.002	1.788	0.182	0.161	3.692	0.360	0.084	0.005	0.001	0.000

References

[1] Energy - Renewable energy - OECD data, URL https://data.oecd.org/chart/6ZhT.

[2] Varone A, Ferrari M. Power to liquid and power to gas: An option for the German Energiewende. Renew Sustain Energy Rev 2015;45:207–18. http://dx.doi.org/10.1016/j.rser.2015.01.049, URL https://www.sciencedirect.com/science/article/pii/S1364032115000593.

[3] Wulf C, Linßen J, Zapp P. Review of power-to-gas projects in Europe. Energy Procedia 2018;155:367–78. http://dx.doi.org/10.1016/j.egypro.2018.11.041, URL https://www.sciencedirect.com/science/article/pii/S1876610218309883.

[4] Shukla P, Skea J, Slade R, Al Khourdajie A, van Diemen R, McCollum D, Pathak M, Some S, Vyas P, Fradera R, Belkacemi M, Hasija A, Lisboa G, Luz S, Malley J. IPCC, 2022: Climate change 2022: Mitigation of climate change. Contribution of working group III to the sixth assessment report of the intergovernmental panel on climate change, Cambridge University Press; 2022, http://dx.doi.org/10.1017/9781009157926, URL https://www.ipcc.ch/report/sixth-assessment-report-working-group-3/.

[5] Blanco H, Nijs W, Ruf J, Faaij A. Potential of Power-to-Methane in the EU energy transition to a low carbon system using cost optimization. Appl Energy 2018;232:323–40. http://dx.doi.org/10.1016/j.apenergy.2018.08.027, URL https://www.sciencedirect.com/science/article/pii/S0306261918311826.

[6] Bos MJ, Kersten SRA, Brilman DWF. Wind power to methanol: Renewable methanol production using electricity, electrolysis of water and CO2 air capture. Appl Energy 2020;264:114672. http://dx.doi.org/10.1016/j.apenergy.2020.114672, URL https://www.sciencedirect.com/science/article/pii/S0306261920301847.

[7] Küngas R, Blennow P, Heiredal-Clausen T, Nørby TH, Rass-Hansen J, Hansen JB, Moses PG. Power-to-X activities at Haldor Topsoe: our approach for electrification of the chemicals industry. Zenodo; 2021, http://dx.doi.org/10.5281/zenodo.5115854, URL https://zenodo.org/record/5115854.

[8] Supronowicz W, A. Ignatyev I, Lolli G, Wolf A, Zhao L, Mleczko L. Formic acid: a future bridge between the power and chemical industries. Green Chem 2015;17(5):2904–11. http://dx.doi.org/10.1039/C5GC00249D, URL https://pubs.rsc.org/en/content/articlelanding/2015/gc/c5gc00249d, Publisher: Royal Society of Chemistry.

[9] Chatterjee S, Dutta I, Lum Y, Lai Z, Huang K-W. Enabling storage and utilization of low-carbon electricity: power to formic acid. Energy Environ Sci 2021;14(3):1194–246. http://dx.doi.org/10.1039/D0EE03011B, URL https://pubs.rsc.org/en/content/articlelanding/2021/ee/d0ee03011b, Publisher: Royal Society of Chemistry.

[10] Dutta I, Chatterjee S, Cheng H, Parsapur RK, Liu Z, Li Z, Ye E, Kawanami H, Low JSC, Lai Z, Loh XJ, Huang K-W. Formic acid to power towards low-carbon economy. Adv Energy Mater 2022;12(15):2103799. http://dx.doi.org/10.1002/aenm.202103799, URL https://onlinelibrary.wiley.com/doi/abs/10.1002/aenm.202103799 _eprint: https://onlinelibrary.wiley.com/doi/pdf/10.1002/aenm.202103799.

[11] Bergthorson JM. Recyclable metal fuels for clean and compact zero-carbon power. Prog Energy Combust Sci 2018;68:169–96. http://dx.doi.org/10.1016/j.pecs.2018.05.001, URL https://www.sciencedirect.com/science/article/pii/S0360128518300327.

[12] Kuhn C, Düll A, Rohlfs P, Tischer S, Börnhorst M, Deutschmann O. Iron as recyclable energy carrier: Feasibility study and kinetic analysis of iron oxide reduction. Appl Energy Combust Sci 2022;12:100096. http://dx.doi.org/10.1016/j.jaecs.2022.100096, URL https://www.sciencedirect.com/science/article/pii/S2666352X22000395.

[13] Møller KT, Sheppard D, Ravnsbæk DB, Buckley CE, Akiba E, Li H-W, Jensen TR. Complex metal hydrides for hydrogen, thermal and electrochemical energy storage. Energies 2017;10(10):1645. http://dx.doi.org/10.3390/en10101645, URL https://www.mdpi.com/1996-1073/10/10/1645 Number: 10 Publisher: Multidisciplinary Digital Publishing Institute.

[14] Düll A, Rohlfs P, Deutschmann O, Börnhorst M. Performance evaluation of KBH4 as energy carrier for shipping applications. Chem Ing Tech 2022;94(5):747–59. http://dx.doi.org/10.1002/cite.202100193, URL https://onlinelibrary.wiley.com/doi/abs/10.1002/cite.202100193 _eprint: https://onlinelibrary.wiley.com/doi/pdf/10.1002/cite.202100193.

[15] Imports of natural gas by partner country | Eurostat. 2023, URL https://ec.europa.eu/eurostat/databrowser/view/nrg_ti_gas/default/table?lang=en.

[16] System development map, URL https://www.gie.eu/publications/maps/system-development-map/.

[17] Sustainable aviation fuels, URL https://www.energy.gov/eere/bioenergy/sustainable-aviation-fuels.

[18] Sterner M, Stadler I. Energiespeicher - Bedarf, technologien, integration. Berlin, Heidelberg: Springer Berlin Heidelberg; 2014, http://dx.doi.org/10.1007/978-3-642-37380-0, URL http://link.springer.com/10.1007/978-3-642-37380-0.

[19] Thema M, Bauer F, Sterner M. Power-to-Gas: Electrolysis and methanation status review. Renew Sustain Energy Rev 2019;112:775–87. http://dx.doi.org/10.1016/j.rser.2019.06.030, URL https://www.sciencedirect.com/science/article/pii/S136403211930423X.

[20] Martin MR, Fornero JJ, Stark R, Mets L, Angenent LT. A single-culture bioprocess of *methanothermobacter thermautotrophicus* to upgrade digester biogas by CO_2-to-CH_4 conversion with H_2. Archaea 2013;2013:e157529. http://dx.doi.org/10.1155/2013/157529, URL https://www.hindawi.com/journals/archaea/2013/157529/, Publisher: Hindawi.

[21] Bailera M, Lisbona P, Romeo LM, Espatolero S. Power to Gas projects review: Lab, pilot and demo plants for storing renewable energy and CO2. Renew Sustain Energy Rev 2017;69:292–312. http://dx.doi.org/10.1016/j.rser.2016.11.130, URL https://www.sciencedirect.com/science/article/pii/S1364032116307833.

[22] Carmeuse, ENGIE and John Cockerill join forces to reduce industrial CO2 emissions in Wallonia. 2020, URL https://www.carmeuse.com/eu-en/newsroom/global/carmeuse-engie-and-john-cockerill-join-forces-reduce-industrial-co2-emissions.

[23] Review EI. Electrochaea and the European innovation council accelerate rollout of biological methanation technology. 2021, URL https://energyindustryreview.com/power/electrochaea-and-the-european-innovation-council-accelerate-rollout-of-biological-methanation-technology/.

[24] Gruber M, Weinbrecht P, Biffar L, Harth S, Trimis D, Brabandt J, Posdziech O, Blumentritt R. Power-to-Gas through thermal integration of high-temperature steam electrolysis and carbon dioxide methanation - Experimental results. Fuel Process Technol 2018;181:61–74. http://dx.doi.org/10.1016/j.fuproc.2018.09.003, URL https://www.sciencedirect.com/science/article/pii/S037838201831155X.

[25] Becker WL, Penev M, Braun RJ. Production of synthetic natural gas from carbon dioxide and renewably generated hydrogen: A techno-economic analysis of a power-to-gas strategy. J Energy Resour Technol 2018;141(2). http://dx.doi.org/10.1115/1.4041381.

[26] Guilera J, Ramon Morante J, Andreu T. Economic viability of SNG production from power and CO2. Energy Convers Manage 2018;162:218–24. http://dx.doi.org/10.1016/j.enconman.2018.02.037, URL https://www.sciencedirect.com/science/article/pii/S019689041830147X.

[27] Electrolysers – analysis, URL https://www.iea.org/reports/electrolysers.

[28] GrInHy2.0 - green industrial hydrogen via steam electrolysis. 2022, URL https://www.green-industrial-hydrogen.com/.

[29] Sunfire. Renewable Hydrogen Project "MultiPLHY": World's largest high-temperature electrolyzer from sunfire successfully installed. 2023, URL https://www.sunfire.de/en/news/detail/renewable-hydrogen-project-multiplhy-worlds-largest-high-temperature-electrolyzer-from-sunfire-successfully-installed. [Accessed 24 April 2023].

[30] Brisse A, Schefold J, Zahid M. High temperature water electrolysis in solid oxide cells. Int J Hydrog Energy 2008;33(20):5375–82. http://dx.doi.org/10.1016/j.ijhydene.2008.07.120, URL https://www.sciencedirect.com/science/article/pii/S0360319908008355.

[31] Mogensen MB. Thermodynamics of high temperature H2O and CO2 electrolysis. 2020, 4887975. http://dx.doi.org/10.6084/M9.FIGSHARE.12652322.V1, URL https://figshare.com/articles/Thermodynamics_of_high_temperature_H2O_and_CO2_electrolysis/12652322/1, BytesArtwork Size: 4887975 Bytes Publisher: figshare.

[32] Sunfire - World's largest high-temperature electrolyzer achieves record efficiency, URL https://www.sunfire.de/en/news/detail/worlds-largest-high-temperature-electrolyzer-achieves-record-efficiency.

[33] SUNFIRE-HYLINK SOEC, URL https://www.sunfire.de/files/sunfire/images/content/Sunfire.de%20(neu)/Sunfire-Factsheet-HyLink-SOEC-20210303.pdf.

[34] Nel - PEM electrolyser. 2018, URL https://nelhydrogen.com/product/m-series-3/.

[35] Nel - atmospheric alkaline electrolyser. 2018, URL https://nelhydrogen.com/product/atmospheric-alkaline-electrolyser-a-series/.

[36] Buttler A, Spliethoff H. Current status of water electrolysis for energy storage, grid balancing and sector coupling via power-to-gas and power-to-liquids: A review. Renew Sustain Energy Rev 2018;82:2440–54. http://dx.doi.org/10.1016/j.rser.2017.09.003, URL https://linkinghub.elsevier.com/retrieve/pii/S136403211731242X.

[37] Anghilante R, Müller C, Schmid M, Colomar D, Ortloff F, Spörl R, Brisse A, Graf F. Innovative power-to-gas plant concepts for upgrading of gasification biosyngas through steam electrolysis and catalytic methanation. Energy Convers Manage 2019;183:462–73. http://dx.doi.org/10.1016/j.enconman.2018.12.101, URL https://linkinghub.elsevier.com/retrieve/pii/S0196890419300172.

[38] Wang L, Pérez-Fortes M, Madi H, Diethelm S, herle JV, Maréchal F. Optimal design of solid-oxide electrolyzer based power-to-methane systems: A comprehensive comparison between steam electrolysis and co-electrolysis. Appl Energy 2018;211:1060–79. http://dx.doi.org/10.1016/j.apenergy.2017.11.050, Publisher: Elsevier Ltd.

[39] Hauch A, Küngas R, Blennow P, Hansen AB, Hansen JB, Mathiesen BV, Mogensen MB. Recent advances in solid oxide cell technology for electrolysis. Science 2020;370(6513):eaba6118. http://dx.doi.org/10.1126/science.aba6118, URL https://www.science.org/doi/full/10.1126/science.aba6118, Publisher: American Association for the Advancement of Science.

[40] Metz B, Davidson O, de Coninck H, Loos M, Meyer L. IPCC special report on carbon dioxide capture and storage. Tech. rep., Intergovernmental Panel on Climate Change; 2005.

[41] Nagireddi S, Agarwal JR, Vedapuri D. Carbon dioxide capture, utilization, and sequestration: Current status, challenges, and future prospects for global decarbonization. ACS Eng Au 2024;4(1):22–48. http://dx.doi.org/10.1021/acsengineeringau.3c00049, URL https://pubs.acs.org/doi/10.1021/acsengineeringau.3c00049.

[42] Leonzio G, Zondervan E. Analysis and optimization of carbon supply chains integrated to a power to gas process in Italy. J Clean Prod 2020;269:122172. http://dx.doi.org/10.1016/j.jclepro.2020.122172, URL https://linkinghub.elsevier.com/retrieve/pii/S0959652620322198.

[43] Lux B, Gegenheimer J, Franke K, Sensfuß F, Pfluger B. Supply curves of electricity-based gaseous fuels in the MENA region. Comput Ind Eng 2021;162:107647. http://dx.doi.org/10.1016/j.cie.2021.107647, URL https://www.sciencedirect.com/science/article/pii/S0360835221005519.

[44] Wang M, Lawal A, Stephenson P, Sidders J, Ramshaw C. Post-combustion CO2 capture with chemical absorption: A state-of-the-art review. Chem Eng Res Des 2011;89(9):1609–24. http://dx.doi.org/10.1016/j.cherd.2010.11.005, URL https://linkinghub.elsevier.com/retrieve/pii/S0263876210003345.

[45] Bioenergy with carbon capture and storage – analysis, URL https://www.iea.org/reports/bioenergy-with-carbon-capture-and-storage.

[46] Khan MU, Lee JTE, Bashir MA, Dissanayake PD, Ok YS, Tong YW, Shariati MA, Wu S, Ahring BK. Current status of biogas upgrading for direct biomethane use: A review. Renew Sustain Energy Rev 2021;149:111343. http://dx.doi.org/10.1016/j.rser.2021.111343, URL https://www.sciencedirect.com/science/article/pii/S1364032121006298.

[47] Çelik A, Othman IB, Müller H, Lott P, Deutschmann O. Pyrolysis of biogas for carbon capture and carbon dioxide-free production of hydrogen. React Chem Eng 2023. http://dx.doi.org/10.1039/D3RE00360D, URL https://pubs.rsc.org/en/content/articlelanding/2023/re/d3re00360d, Publisher: Royal Society of Chemistry.

[48] Lovett AA, Sünnenberg GM, Richter GM, Dailey AG, Riche AB, Karp A. Land use implications of increased biomass production identified by GIS-based suitability and yield mapping for miscanthus in England. BioEnergy Res 2009;2(1):17–28. http://dx.doi.org/10.1007/s12155-008-9030-x.

[49] de Coninck H, Revi A, Babiker M, Bertoldi P, Buckeridge M, Cartwright A, Dong W, Ford J, Fuss J, Hourcade J-C, Ley D, Mechler R, Newmann P, Revokatowa A, Schultz S, Steg L, Sugiyama T. Strengthening and implementing the global response. In: Global warming of 1.5° c. an IPCC special report on the impacts of global warming of 1.5° c above pre-industrial levels and related global greenhouse gas emission pathways, in the context of strengthening the global response to the threat of climate change, sustainable development, and efforts to eradicate poverty. 2018, URL https://www.ipcc.ch/sr15/chapter/chapter-4/.

[50] Wurzbacher J. Capturing CO2 from air. In: Liebl J, Beidl C, editors. Internationaler motorenkongress 2017. Wiesbaden: Springer Fachmedien Wiesbaden; 2017, p. 499–511. http://dx.doi.org/10.1007/978-3-658-17109-4_32, URL http://link.springer.com/10.1007/978-3-658-17109-4_32, Series Title: Proceedings.

[51] McQueen N, Gomes KV, McCormick C, Blumanthal K, Pisciotta M, Wilcox J. A review of direct air capture (DAC): scaling up commercial technologies and innovating for the future. Prog Energy 2021;3(3):032001. http://dx.doi.org/10.1088/2516-1083/abf1ce, URL https://iopscience.iop.org/article/10.1088/2516-1083/abf1ce.

[52] Bellini R, Bassani I, Vizzarro A, Azim AA, Vasile NS, Pirri CF, Verga F, Menin B. Biological aspects, advancements and techno-economical evaluation of biological methanation for the recycling and valorization of CO2. Energies 2022;15(11):4064. http://dx.doi.org/10.3390/en15114064, URL https://www.mdpi.com/1996-1073/15/11/4064, Number: 11 Publisher: Multidisciplinary Digital Publishing Institute.

[53] Rehmat A, Randhava SS. Selective methanation of carbon monoxide. Prod RD 1970;9(4):512–5. http://dx.doi.org/10.1021/i360036a009, Publisher: American Chemical Society.

[54] Schmider D, Maier L, Deutschmann O. Reaction kinetics of CO and CO2 methanation over nickel. Ind Eng Chem Res 2021;60(16):5792–805. http://dx.doi.org/10.1021/acs.iecr.1c00389, Publisher: American Chemical Society.

[55] Rönsch S, Schneider J, Matthischke S, Schlüter M, Götz M, Lefebvre J, Prabhakaran P, Bajohr S. Review on methanation – From fundamentals to current projects. Fuel 2016;166:276–96. http://dx.doi.org/10.1016/j.fuel.2015.10.111, URL https://www.sciencedirect.com/science/article/pii/S0016236115011254.

[56] Schaaf T, Grünig J, Schuster MR, Rothenfluh T, Orth A. Methanation of CO2 - storage of renewable energy in a gas distribution system. Energy Sustain Soc 2014;4(1):2. http://dx.doi.org/10.1186/s13705-014-0029-1.

[57] Lefebvre J. Three-phase CO2 methanation: methanation reaction kinetics and transient behavior of a slurry bubble column reactor (Ph.D. thesis), München: Verlag Dr. Hut; 2019.

[58] Schollenberger D, Bajohr S, Gruber M, Reimert R, Kolb T. Scale-Up of innovative honeycomb reactors for power-to-gas applications – The project store&go. Chem Ing Tech 2018;90(5):696–702. http://dx.doi.org/10.1002/cite.201700139, URL https://onlinelibrary.wiley.com/doi/abs/10.1002/cite.201700139, _eprint: https://onlinelibrary.wiley.com/doi/pdf/10.1002/cite.201700139.

[59] Ghaib K, Ben-Fares F-Z. Power-to-Methane: A state-of-the-art review. Renew Sustain Energy Rev 2018;81:433–46. http://dx.doi.org/10.1016/j.rser.2017.08.004, URL https://linkinghub.elsevier.com/retrieve/pii/S1364032117311346.

[60] Hidalgo D, Martín-Marroquín J. Power-to-methane, coupling CO2 capture with fuel production: An overview. Renew Sustain Energy Rev 2020;132:110057. http://dx.doi.org/10.1016/j.rser.2020.110057, URL https://linkinghub.elsevier.com/retrieve/pii/S1364032120303488.

[61] Wendel CH, Kazempoor P, Braun RJ. Novel electrical energy storage system based on reversible solid oxide cells: System design and operating conditions. J Power Sources 2015;276:133–44. http://dx.doi.org/10.1016/j.jpowsour.2014.10.205, URL https://www.sciencedirect.com/science/article/pii/S0378775314018242.

[62] Reznicek E, Braun RJ. Techno-economic and off-design analysis of stand-alone, distributed-scale reversible solid oxide cell energy storage systems. Energy Convers Manage 2018;175:263–77. http://dx.doi.org/10.1016/j.enconman.2018.08.087, URL https://linkinghub.elsevier.com/retrieve/pii/S019689041830952X.

[63] Jeanmonod G, Wang L, Diethelm S, Maréchal F, Van herle J. Trade-off designs of power-to-methane systems via solid-oxide electrolyzer and the application to biogas upgrading. Appl Energy 2019;247:572–81. http://dx.doi.org/10.1016/j.apenergy.2019.04.055, URL https://www.sciencedirect.com/science/article/pii/S0306261919307020.

[64] Wang L, Düll J, Maréchal F, Van herle J. Trade-off designs and comparative exergy evaluation of solid-oxide electrolyzer based power-to-methane plants. Int J Hydrog Energy 2019;44(19):9529–43. http://dx.doi.org/10.1016/j.ijhydene.2018.11.151, URL https://www.sciencedirect.com/science/article/pii/S0360319918337832.

[65] Wang L, Rao M, Diethelm S, Lin TE, Zhang H, Hagen A, Maréchal F, Van herle J. Power-to-methane via co-electrolysis of H2O and CO2: The effects of pressurized operation and internal methanation. Appl Energy 2019;250:1432–45. http://dx.doi.org/10.1016/j.apenergy.2019.05.098, Publisher: Elsevier Ltd.

[66] Jalili M, Ghazanfari Holagh S, Chitsaz A, Song J, Markides CN. Electrolyzer cell-methanation/Sabatier reactors integration for power-to-gas energy storage: Thermo-economic analysis and multi-objective optimization. Appl Energy 2023;329:120268. http://dx.doi.org/10.1016/j.apenergy.2022.120268, URL https://www.sciencedirect.com/science/article/pii/S0306261922015252.

[67] Uebbing J, Rihko-Struckmann L, Sager S, Sundmacher K. CO2 methanation process synthesis by superstructure optimization. J CO2 Util 2020;40:101228. http://dx.doi.org/10.1016/j.jcou.2020.101228, URL https://www.sciencedirect.com/science/article/pii/S221298202030278X.

[68] Gassner M, Maréchal F. Thermo-economic optimisation of the integration of electrolysis in synthetic natural gas production from wood. Energy 2008;33(2):189–98. http://dx.doi.org/10.1016/j.energy.2007.09.010, URL https://www.sciencedirect.com/science/article/pii/S0360544207001764.

[69] Safari F, Dincer I. Assessment and optimization of an integrated wind power system for hydrogen and methane production. Energy Convers Manage 2018;177:693–703. http://dx.doi.org/10.1016/j.enconman.2018.09.071, URL https://www.sciencedirect.com/science/article/pii/S0196890418310744.

[70] Gorre J, Ortloff F, van Leeuwen C. Production costs for synthetic methane in 2030 and 2050 of an optimized Power-to-Gas plant with intermediate hydrogen storage. Appl Energy 2019;253:113594. http://dx.doi.org/10.1016/j.apenergy.2019.113594, URL https://www.sciencedirect.com/science/article/pii/S0306261919312681.

[71] Morgenthaler S, Ball C, Koj JC, Kuckshinrichs W, Witthaut D. Site-dependent levelized cost assessment for fully renewable Power-to-Methane systems. Energy Convers Manage 2020;223:113150. http://dx.doi.org/10.1016/j.enconman.2020.113150, URL https://linkinghub.elsevier.com/retrieve/pii/S0196890420306944.

[72] Chi Y, Hu Q, Lin J, Qiu Y, Mu S, Li W, Song Y. Numerical simulation acceleration of flat-chip solid oxide cell stacks by data-driven surrogate cell submodels. J Power Sources 2023;553:232255. http://dx.doi.org/10.1016/j.jpowsour.2022.232255, URL https://www.sciencedirect.com/science/article/pii/S0378775322012320.

[73] Chi Y, Yokoo K, Nakajima H, Ito K, Lin J, Song Y. Optimizing the homogeneity and efficiency of a solid oxide electrolysis cell based on multiphysics simulation and data-driven surrogate model. J Power Sources 2023;562:232760. http://dx.doi.org/10.1016/j.jpowsour.2023.232760, URL https://www.sciencedirect.com/science/article/pii/S0378775323001350.

[74] Qi M, Lee J, Hong S, Kim J, Liu Y, Park J, Moon I. Flexible and efficient renewable-power-to-methane concept enabled by liquid CO2 energy storage: Optimization with power allocation and storage sizing. Energy 2022;256:124583. http://dx.doi.org/10.1016/j.energy.2022.124583, URL https://www.sciencedirect.com/science/article/pii/S0360544222014864.

[75] Koytsoumpa EI, Karellas S, Kakaras E. Modelling of Substitute Natural Gas production via combined gasification and power to fuel. Renew Energy 2019;135:1354–70. http://dx.doi.org/10.1016/j.renene.2018.09.064, URL https://www.sciencedirect.com/science/article/pii/S0960148118311273.

[76] Drechsler C, Agar DW. Intensified integrated direct air capture - power-to-gas process based on H2O and CO2 from ambient air. Appl Energy 2020;273:115076. http://dx.doi.org/10.1016/j.apenergy.2020.115076, URL https://www.sciencedirect.com/science/article/pii/S0306261920305882.

[77] Martínez I, Romano MC. Flexible sorption enhanced gasification (SEG) of biomass for the production of synthetic natural gas (SNG) and liquid biofuels: Process assessment of stand-alone and power-to-gas plant schemes for SNG production. Energy 2016;113:615–30. http://dx.doi.org/10.1016/j.energy.2016.07.026, URL https://www.sciencedirect.com/science/article/pii/S0360544216309501.

[78] Coppitters D, Costa A, Chauvy R, Dubois L, De Paepe W, Thomas D, De Weireld G, Contino F. Energy, exergy, economic and environmental (4E) analysis of integrated direct air capture and CO2 methanation under uncertainty. Fuel 2023;344:127969. http://dx.doi.org/10.1016/j.fuel.2023.127969, URL https://www.sciencedirect.com/science/article/pii/S0016236123005823.

[79] Perpiñán J, Bailera M, Peña B, Romeo LM, Eveloy V. Technical and economic assessment of iron and steelmaking decarbonization via power to gas and amine scrubbing. Energy 2023;276:127616. http://dx.doi.org/10.1016/j.energy.2023.127616, URL https://www.sciencedirect.com/science/article/pii/S0360544223010101.

[80] Peters R, Baltruweit M, Grube T, Samsun RC, Stolten D. A techno economic analysis of the power to gas route. J CO2 Util 2019;34:616–34. http://dx.doi.org/10.1016/j.jcou.2019.07.009, URL https://linkinghub.elsevier.com/retrieve/pii/S2212982019304731.

[81] Zhu H, Kee RJ, Janardhanan VM, Deutschmann O, Goodwin DG. Modeling elementary heterogeneous chemistry and electrochemistry in solid-oxide fuel cells. J Electrochem Soc 2005;152(12):A2427. http://dx.doi.org/10.1149/1.2116607, URL https://iopscience.iop.org/article/10.1149/1.2116607.

[82] Wehrle L, Schmider D, Dailly J, Banerjee A, Deutschmann O. Benchmarking solid oxide electrolysis cell-stacks for industrial Power-to-Methane systems via hierarchical multi-scale modelling. Appl Energy 2022;317:119143. http://dx.doi.org/10.1016/j.apenergy.2022.119143, URL https://www.sciencedirect.com/science/article/pii/S0306261922005190.

[83] Khan MI, Yasmin T, Shakoor A. Technical overview of compressed natural gas (CNG) as a transportation fuel. Renew Sustain Energy Rev 2015;51:785–97. http://dx.doi.org/10.1016/j.rser.2015.06.053, URL https://www.sciencedirect.com/science/article/pii/S1364032115006255.

[84] Sun L, Wang Y, Guan N, Li L. Methane activation and utilization: Current status and future challenges. Energy Technol 2020;8(8):1900826. http://dx.doi.org/10.1002/ente.201900826, URL https://onlinelibrary.wiley.com/doi/abs/10.1002/ente.201900826, _eprint: https://onlinelibrary.wiley.com/doi/pdf/10.1002/ente.201900826.

[85] Qi M, Liu Y, He T, Yin L, Shu C-M, Moon I. System perspective on cleaner technologies for renewable methane production and utilisation towards carbon neutrality: Principles, techno-economics, and carbon footprints. Fuel 2022;327:125130. http://dx.doi.org/10.1016/j.fuel.2022.125130, URL https://www.sciencedirect.com/science/article/pii/S0016236122019718.

[86] DIN EN 16726:2019-11, gasinfrastruktur_- beschaffenheit von gas_- gruppe_H; deutsche fassung EN_16726:2015+A1:2018. Tech. rep., Beuth Verlag GmbH, http://dx.doi.org/10.31030/2867769, URL https://www.beuth.de/de/-/-/292011490.

[87] Gröschl F. Daten und fakten gas-mobilität PKW, LKW, bus. 2018, URL https://www.dvgw.de/leistungen/publikationen/publikationsliste/daten-und-fakten-erdgasmobilitaet.

[88] Ebrahim M, Kawari A. Pinch technology: an efficient tool for chemical-plant energy and capital-cost saving. Appl Energy 2000;65(1):45–9. http://dx.doi.org/10.1016/S0306-2619(99)00057-4, URL https://www.sciencedirect.com/science/article/pii/S0306261999000574.

[89] Im-orb K, Arpornwichanop A. Comparative techno-economic assessment of bio-methanol and bio-DME production from oil palm residue. Energy Convers Manage 2022;258:115511. http://dx.doi.org/10.1016/j.enconman.2022.115511, URL https://www.sciencedirect.com/science/article/pii/S0196890422003077.

[90] Bou Malham C, Zoughaib A, Rivera Tinoco R, Schuhler T. Hybrid optimization methodology (exergy/pinch) and application on a simple process. Energies 2019;12(17):3324. http://dx.doi.org/10.3390/en12173324, URL https://www.mdpi.com/1996-1073/12/17/3324, Number: 17 Publisher: Multidisciplinary Digital Publishing Institute.

[91] Parra D, Zhang X, Bauer C, Patel MK. An integrated techno-economic and life cycle environmental assessment of power-to-gas systems. Appl Energy 2017;193:440–54. http://dx.doi.org/10.1016/j.apenergy.2017.02.063, URL https://www.sciencedirect.com/science/article/pii/S0306261917302064.

[92] Perna A, Moretti L, Ficco G, Spazzafumo G, Canale L, Dell'Isola M. SNG generation via power to gas technology: Plant design and annual performance assessment. Appl Sci 2020;10(23):8443. http://dx.doi.org/10.3390/app10238443, URL https://www.mdpi.com/2076-3417/10/23/8443, Number: 23 Publisher: Multidisciplinary Digital Publishing Institute.

[93] Deutz S, Bardow A. Life-cycle assessment of an industrial direct air capture process based on temperature–vacuum swing adsorption. Nat Energy 2021;6(2):203–13. http://dx.doi.org/10.1038/s41560-020-00771-9, URL http://www.nature.com/articles/s41560-020-00771-9.

[94] Zhao B, Liu F, Cui Z, Liu C, Yue H, Tang S, Liu Y, Lu H, Liang B. Enhancing the energetic efficiency of MDEA/PZ-based CO2 capture technology for a 650MW power plant: Process improvement. Appl Energy 2017;185:362–75. http://dx.doi.org/10.1016/j.apenergy.2016.11.009, URL https://www.sciencedirect.com/science/article/pii/S0306261916315951.

[95] Müller C, Ortloff F, Graf F. Final report of the baden-wurttemberg project Res2CNG - innovative production of SNG and CNG from biogenic waste and residues. 2018, URL https://pudi.lubw.de/detailseite/-/publication/92291.

[96] Wurzbacher JA, Gebald C, Brunner S, Steinfeld A. Heat and mass transfer of temperature–vacuum swing desorption for CO2 capture from air. Chem Eng J 2016;283:1329–38. http://dx.doi.org/10.1016/j.cej.2015.08.035, URL https://linkinghub.elsevier.com/retrieve/pii/S138589471501116X.

[97] Ibrahim AY, Ashour FH, Ghallab AO, Ali M. Effects of piperazine on carbon dioxide removal from natural gas using aqueous methyl diethanol amine. J Natl Gas Sci Eng 2014;21:894–9. http://dx.doi.org/10.1016/j.jngse.2014.10.011, URL https://www.sciencedirect.com/science/article/pii/S1875510014003102.

[98] Frailie PT. Modeling of carbon dioxide absorption/stripping by aqueous methyldiethanolamine/piperazine (Thesis), Austin: University of Texas; 2014, URL https://repositories.lib.utexas.edu/handle/2152/25019, [Accepted: 2014-07-03T20:58:39Z].

[99] Svensson H, Hulteberg C, Karlsson HT. Heat of absorption of CO2 in aqueous solutions of N-methyldiethanolamine and piperazine. Int J Greenh Gas Control 2013;17:89–98. http://dx.doi.org/10.1016/j.ijggc.2013.04.021, URL https://www.sciencedirect.com/science/article/pii/S1750583613002016.

[100] Bartholomew CH, Weatherbee GD, Jarvi GA. Sulfur poisoning of nickel methanation catalysts: I. in situ deactivation by H2S of nickel and nickel bimetallics. J Catal 1979;60(2):257–69. http://dx.doi.org/10.1016/0021-9517(79)90147-7, URL https://www.sciencedirect.com/science/article/pii/0021951779901477.

[101] Robinson VS. Process for desulfurization using particulate zinc oxide shapes of high surface area and improved strength. 1978, URL https://patents.google.com/patent/US4128619/en.

[102] Solarte-Toro JC, González-Aguirre JA, Poveda Giraldo JA, Cardona Alzate CA. Thermochemical processing of woody biomass: A review focused on energy-driven applications and catalytic upgrading. Renew Sustain Energy Rev 2021;136:110376. http://dx.doi.org/10.1016/j.rser.2020.110376, URL https://linkinghub.elsevier.com/retrieve/pii/S136403212030664X.

[103] García R, Pizarro C, Lavín AG, Bueno JL. Biomass sources for thermal conversion. Techno-economical overview. Fuel 2017;195:182–9. http://dx.doi.org/10.1016/j.fuel.2017.01.063, URL https://www.sciencedirect.com/science/article/pii/S0016236117300698.

[104] Anghilante R. Flexibilisation and integration of solid oxide electrolysis units in power to synthetic natural gas plants (Ph.D. thesis), Toulouse: Institut national polytechnique; 2020, URL http://www.theses.fr/2020INPT0094/document.

[105] Schmid M, Beirow M, Schweitzer D, Waizmann G, Spörl R, Scheffknecht G. Product gas composition for steam-oxygen fluidized bed gasification of dried sewage sludge, straw pellets and wood pellets and the influence of limestone as bed material. Biomass Bioenergy 2018;117:71–7. http://dx.doi.org/10.1016/j.biombioe.2018.07.011, URL https://linkinghub.elsevier.com/retrieve/pii/S0961953418301752.

[106] Koytsoumpa EI, Karellas S. Equilibrium and kinetic aspects for catalytic methanation focusing on CO2 derived Substitute Natural Gas (SNG). Renew Sustain Energy Rev 2018;94:536–50. http://dx.doi.org/10.1016/j.rser.2018.06.051, URL https://linkinghub.elsevier.com/retrieve/pii/S1364032118304878.

[107] Jensen JH, Poulsen JM, Andersen NU. From coal to clean energy. In: Nitrogen+syngas. Vol. 310, 2011, p. 34–8.

[108] Siegfried DB, Frank D-IG, Rainer PDR. Methansynthese in einem Blasensäulenreaktor. 2012, URL https://patents.google.com/patent/DE102011009163A1/en?oq=three+phase+methanation.

[109] Lefebvre J, Götz M, Bajohr S, Reimert R, Kolb T. Improvement of three-phase methanation reactor performance for steady-state and transient operation. Fuel Process Technol 2015;132:83–90. http://dx.doi.org/10.1016/j.fuproc.2014.10.040, URL https://www.sciencedirect.com/science/article/pii/S0378382014004640.

[110] Lefebvre J, Bajohr S, Kolb T. A comparison of two-phase and three-phase CO2 methanation reaction kinetics. Fuel 2019;239:896–904. http://dx.doi.org/10.1016/j.fuel.2018.11.051, URL https://linkinghub.elsevier.com/retrieve/pii/S0016236118319379.

[111] Sauerschell S, Bajohr S, Kolb T. Methanation pilot plant with a slurry bubble column reactor: Setup and first experimental results. Energy Fuels 2022;36(13):7166–76. http://dx.doi.org/10.1021/acs.energyfuels.2c00655, URL https://doi.org/10.1021/acs.energyfuels.2c00655, Publisher: American Chemical Society.

[112] Riedel M, Heddrich M, Ansar A, Fang Q, Blum L, Friedrich K. Pressurized operation of solid oxide electrolysis stacks: An experimental comparison of the performance of 10-layer stacks with fuel electrode and electrolyte supported cell concepts. J Power Sources 2020;475:228682. http://dx.doi.org/10.1016/j.jpowsour.2020.228682, URL https://linkinghub.elsevier.com/retrieve/pii/S0378775320309861.

[113] Nechache A, Hody S. Alternative and innovative solid oxide electrolysis cell materials: A short review. Renew Sustain Energy Rev 2021;149:111322. http://dx.doi.org/10.1016/j.rser.2021.111322, URL https://www.sciencedirect.com/science/article/pii/S1364032121006080.

[114] Kusnezoff M, Trofimenko N, Müller M, Michaelis A. Influence of electrode design and contacting layers on performance of electrolyte supported SOFC/SOEC single cells. Materials 2016;9(11):906. http://dx.doi.org/10.3390/ma9110906, URL https://www.mdpi.com/1996-1944/9/11/906, Number: 11 Publisher: Multidisciplinary Digital Publishing Institute.

[115] Léon A, Micero A, Ludwig B, Brisse A. Effect of scaling-up on the performance and degradation of long-term operated electrolyte supported solid oxide cell, stack and module in electrolysis mode. J Power Sources 2021;510:230346. http://dx.doi.org/10.1016/j.jpowsour.2021.230346, URL https://www.sciencedirect.com/science/article/pii/S0378775321008582.

[116] Chelmehsara ME, Mahmoudimehr J. Techno-economic comparison of anode-supported, cathode-supported, and electrolyte-supported SOFCs. Int J Hydrog Energy 2018;43(32):15521–30. http://dx.doi.org/10.1016/j.ijhydene.2018.06.114, URL https://linkinghub.elsevier.com/retrieve/pii/S0360319918319864.

[117] Deutschmann O, Tischer S, S K, Janardhanan V, Correa C, Chatterjee D, Mladenov N, Minh HD, Karadeniz H, Hettel M, Menon V, Banerjee A, Gossler H, Shirsath A, E D. DETCHEM. 2022, URL https://www.detchem.com.

[118] PROMALIGHT: Rigid microporous insulation boards, URL https://www.promat.com/en/industry/products-solutions/high-temperature-insulation/rigid-panels/promalight/.

[119] Aguiar P, Adjiman CS, Brandon NP. Anode-supported intermediate-temperature direct internal reforming solid oxide fuel cell: II. Model-based dynamic performance and control. J Power Sources 2005;147(1):136–47. http://dx.doi.org/10.1016/j.jpowsour.2005.01.017, URL https://www.sciencedirect.com/science/article/pii/S0378775305001473.

[120] Udagawa J, Aguiar P, Brandon NP. Hydrogen production through steam electrolysis: Model-based steady state performance of a cathode-supported intermediate temperature solid oxide electrolysis cell. J Power Sources 2007;166(1):127–36. http://dx.doi.org/10.1016/j.jpowsour.2006.12.081, URL https://www.sciencedirect.com/science/article/pii/S0378775307001103.

[121] Motylinski K, Wierzbicki M, Kupecki J, Jagielski S. Investigation of off-design characteristics of solid oxide electrolyser (SOE) operating in endothermic conditions. Renew Energy 2021;170:277–85. http://dx.doi.org/10.1016/j.renene.2021.01.097, URL https://www.sciencedirect.com/science/article/pii/S096014812100104X.

[122] Chen H, Wang J, Xu X. Parametric study of operating conditions on performances of a solid oxide electrolysis cell. J Therm Sci 2023. http://dx.doi.org/10.1007/s11630-023-1772-4.

[123] Kim S-D, Seo D-W, Dorai AK, Woo S-K. The effect of gas compositions on the performance and durability of solid oxide electrolysis cells. Int J Hydrog Energy 2013;38(16):6569–76. http://dx.doi.org/10.1016/j.ijhydene.2013.03.115, URL https://www.sciencedirect.com/science/article/pii/S0360319913007556.

[124] Gülich JF. Kreiselpumpen: Handbuch für entwicklung, anlagenplanung und betrieb. 4th ed.. Berlin [u.a.]: Springer; 2013.

[125] Koh J-H, Seo H-K, Lee CG, Yoo Y-S, Lim HC. Pressure and flow distribution in internal gas manifolds of a fuel-cell stack. J Power Sources 2003;115(1):54–65. http://dx.doi.org/10.1016/S0378-7753(02)00615-8, URL https://www.sciencedirect.com/science/article/pii/S0378775302006158.

[126] Belviso C. Zeolites - useful minerals. Rijeka: InTechOpen; 2016.

[127] PDFO - Powell's derivative-free optimization solvers, URL https://www.pdfo.net/.

[128] Powell MJD. Developments of NEWUOA for minimization without derivatives. IMA J Numer Anal 2008;28(4):649–64. http://dx.doi.org/10.1093/imanum/drm047.

[129] Powell MJD. A direct search optimization method that models the objective and constraint functions by linear interpolation. In: Gomez S, Hennart J-P, editors. Advances in optimization and numerical analysis. Mathematics and its applications, Dordrecht: Springer Netherlands; 1994, p. 51–67. http://dx.doi.org/10.1007/978-94-015-8330-5_4.

[130] Nelder JA, Mead R. A simplex method for function minimization. Comput J 1965;7(4):308–13. http://dx.doi.org/10.1093/comjnl/7.4.308.

[131] Henke M, Willich C, Kallo J, Friedrich KA. Theoretical study on pressurized operation of solid oxide electrolysis cells. Int J Hydrog Energy 2014;39(24):12434–9. http://dx.doi.org/10.1016/j.ijhydene.2014.05.185, URL https://www.sciencedirect.com/science/article/pii/S0360319914016012.

[132] Terlouw T, Treyer K, Bauer C, Mazzotti M. Life cycle assessment of direct air carbon capture and storage with low-carbon energy sources. Environ Sci Technol 2021;55(16):11397–411. http://dx.doi.org/10.1021/acs.est.1c03263, Publisher: American Chemical Society.

[133] U.S. Department of Commerce N. Global monitoring laboratory - carbon cycle greenhouse gases. 2023, URL https://gml.noaa.gov/ccgg/trends/.

[134] Wang L, Chen M, Küngas R, Lin T-E, Diethelm S, Maréchal F, Van herle J. Power-to-fuels via solid-oxide electrolyzer: Operating window and techno-economics. Renew Sustain Energy Rev 2019;110:174–87. http://dx.doi.org/10.1016/j.rser.2019.04.071, URL https://www.sciencedirect.com/science/article/pii/S1364032119302928.

[135] Sohal MS, Herring JS. Oxygen handling and cooling options in high temperature electrolysis plants. Tech. rep. INL/EXT-08-14483, Idaho National Lab. (INL), Idaho Falls, ID (United States); 2008, http://dx.doi.org/10.2172/936626, URL https://www.osti.gov/biblio/936626.

[136] Yang Y, Tong X, Hauch A, Sun X, Yang Z, Peng S, Chen M. Study of solid oxide electrolysis cells operated in potentiostatic mode: Effect of operating temperature on durability. Chem Eng J 2021;417:129260. http://dx.doi.org/10.1016/j.cej.2021.129260, URL https://www.sciencedirect.com/science/article/pii/S1385894721008494.

[137] Fasihi M, Efimova O, Breyer C. Techno-economic assessment of CO2 direct air capture plants. J Clean Prod 2019;224:957–80. http://dx.doi.org/10.1016/j.jclepro.2019.03.086, URL https://www.sciencedirect.com/science/article/pii/S0959652619307772.

[138] Chauvy R, Verdonck D, Dubois L, Thomas D, De Weireld G. Techno-economic feasibility and sustainability of an integrated carbon capture and conversion process to synthetic natural gas. J CO2 Util 2021;47:101488. http://dx.doi.org/10.1016/j.jcou.2021.101488, URL https://www.sciencedirect.com/science/article/pii/S221298202100055X.

[139] Coppitters D, Costa A, Dubois L, Thomas D, Weireld GD, Contino F. Robust integration of direct air capture in power-to-methane systems: techno-economic feasibility study under uncertainty. In: Proceedings of ECOS 2022 35th International conference on efficiency, cost, optimization, simulation and environmental impact of energy systems. Vol. 35, 2022, p. 1497.

[140] Furst O, Wehrle L, Schmider D, Dailly J, Deutschmann O. Systematic determination of optimal design-points of fully integrated power-to-SNG process chains via detailed simulation of SOEC stacks. ECS Trans 2023;111(6):1965. http://dx.doi.org/10.1149/11106.1965ecst, URL https://iopscience.iop.org/article/10.1149/11106.1965ecst/meta, Publisher: IOP Publishing.